 CMES, vol.17, no.3, pp.173-203, 2007

Symmetric Variational Formulation of BIE for Domain Decomposition Problems in Elasticity – An SGBEM Approach for Nonconforming Discretizations of Curved Interfaces

R. Vodička[1], V. Mantič[2] and F. París[2]

Abstract: An original approach to solve domain decomposition problems by the symmetric Galerkin boundary element method is developed. The approach, based on a new variational principle for such problems, yields a fully symmetric system of equations. A natural property of the proposed approach is its capability to deal with nonconforming discretizations along straight and curved interfaces, allowing in this way an independent meshing of non-overlapping subdomains to be performed. Weak coupling conditions of equilibrium and compatibility at an interface are obtained from the critical point conditions of the energy functional. Equilibrium is imposed through local traction (Neumann) boundary conditions prescribed on a subdomain situated at one side of the interface, and compatibility is imposed through local displacement (Dirichlet) boundary conditions prescribed on the other subdomain situated at the opposite side of the interface. No additional unknowns such as Lagrange multipliers are introduced. An SGBEM code for 2D elastic domain decomposition problems has been implemented. The effectiveness of the approach developed is documented by numerical examples involving non-matching linear boundary element meshes at the interfaces, where the accuracy is analyzed by comparing the numerical results obtained versus the analytical solutions and by evaluating the convergence rate of the error in the (discretized) integral L_2-norm and maximum-norm for h-refinements of boundary element meshes. Finally, a theoretical analysis of a problem with an interior and an exterior subdomain is introduced to explain the observed behaviour of numerical results.

Keyword: boundary integral equations, boundary elements, SGBEM, domain decomposition, variational formulation, energy functional, nonmatching meshes.

1 Introduction

In the solution of *Boundary Value Problems* (BVPs) of continuum mechanics it is sometimes useful or necessary to split the domain into two or more subdomains, such a procedure being referred to hereinafter as *Domain Decomposition* (DD). DD procedures are usually employed in solving multi-material and contact BVPs or BVPs including complex structures, sometimes with independent modeling of substructures, and in developing algorithms to solve large-scale BVPs on modern parallel computers. DD procedures are also used in coupling different discretization schemes, *e.g. Finite Element Method* (FEM) and *Boundary Element Method* (BEM).

The development of numerical techniques for solution of BVPs via DD (DDBVPs) has substantially increased recently. There exist several ways of mathematical formulation and solution of DDBVPs [Quarteroni and Valli (1999); Steinbach (2003)]. In FEM, special attention is paid to developing techniques based on the mortar element concept; for recent works on application of this approach to elastic and contact problems see McDevitt and Laursen (2000); Puso (2004) and further references given therein. One of the

[1] Technical University of Košice, Faculty of Civil Engineering, Department of Mathematics, Vysokoškolská 4, 042 00 Košice, Slovakia, on leave at[2]

[2] University of Seville, School of Engineering, Group of Elasticity and Strength of Materials, Camino de los Descubrimientos s/n, 41092 Seville, Spain

main problems is to find reliable methods tying nonconforming meshes along curved interfaces; in fact most of the works on mortar techniques have been restricted to straight/planar interfaces. The capability of a DD approach to deal with such discretizations represents an important advantage for engineering applications.

Similar techniques are also under development in BEM [Blázquez *et al.* (1998); Hsiao *et al.* (2000a); González and Abascal (2000); Vodička (2000); Blázquez *et al.* (2002)], only the unknowns along the external boundary and along the interfaces of subdomains being directly computed. The application of DD in BEM is in fact required when solving multi-material BVPs. *Symmetric Galerkin BEM* (SGBEM) [Sirtori (1979); Bonnet *et al.* (1998)] represents a valuable alternative to the classical collocational BEM as it combines the boundary character of the collocational BEM with the symmetrical and energy based formulation typical for FEM. Several techniques have been developed by different authors [Maier *et al.* (1991); Gray and Paulino (1997); Ganguly *et al.* (1999); Vodička (2000); Panzeca *et al.* (2002)] for application of SGBEM to DD and contact BVPs. It is expected that SGBEM will also enable an easy and straightforward coupling with FEM [Hsiao *et al.* (2000b); Han and Atluri (2002); Ganguly *et al.* (2004); Springhetti *et al.* (2004)]. Some other advanced applications of SGBEM can be found in Aimi *et al.* (2003); Qian *et al.* (2004) and Duddeck (2006).

A natural way to formulate SGBEM is a variational formulation, which provides SGBEM with some aspects analogous to FEM, *e.g.* conditions of a critical point of an energy functional represent the final system of equations to be solved and a convergence of error in energy norms can be relatively easily shown [Wendland and Hsiao (2004)]. Thus, it is worth an effort to deduce a variational formulation of SGBEM for DDBVPs. This has been done in the present work by generalizing to DDBVPs, through the development of an original approach, a variational formulation of one-domain SGBEM due to Bonnet (1995).

A variational formulation of a DDBVP requires an adequate formulation of the coupling conditions along the interface. In the present work, it arises from a weak formulation of elastic contact conditions proposed by Blázquez *et al.* (1998) (developing an original idea by Schnack (1987)), here adapted for DDBVP with perfect interfaces. In fact, the variational principle proposed produces the weak coupling conditions as a natural generalization of the classical strong point-wise coupling conditions, in such a way that the developed approach shares some ideas with the mortar approaches used in FEM [McDevitt and Laursen (2000); Puso (2004)].

An implementation of the above weak formulation of coupling conditions for non-matching boundary element meshes at curved interfaces has been included in the SGBEM code developed. Various methods of data transfer between non-matching meshes via integrals computing over the discretized curved surfaces were introduced in Jiao and Heath (2004), one of these methods based on the concept of common refinement having been used in the present code.

The structure of the present paper is as follows. Elastic BVP and DDBVP together with the two basic *Boundary Integral Equations* (BIEs) are introduced in the preliminary Section 2. In Section 3 the main theoretical results are presented. After introducing the functional of the energy for DDBVPs, it is shown that its critical point gives the solution of the original DDBVP. The resulting weak formulation of the BIE system, whose solution corresponds to this critical point, is first deduced in the integral form. Then, an operator notation is used to show easily its overall symmetrical structure. The discretization of the BIE system obtained by SGBEM, using linear continuous boundary elements, is introduced in Section 4. The accuracy and convergence for h-refinements of the present approach are documented in Section 5 by three numerical examples. In order to explain some aspects of the observed behaviour of the numerical results, a theoretical analysis of a simple DDBVP, with a bounded interior and an unbounded exterior subdomain, at the discretized level, is presented in the Appendix, where a reduction of the resulting system matrix to its Schur complement is carried out and the obtained matrix

operators, which include Galerkin discretizations of the local Steklov-Poincaré operators for subdomains [Quarteroni and Valli (1999); Hsiao *et al.* (2000b); Steinbach (2003)], are discussed.

2 Preliminaries.

2.1 Elastic BVP

Let us consider a linear elastic body defined by a domain $\Omega \subset \mathbb{R}^d$ $(d = 2 \text{ or } 3)$ with a bounded Lipschitz boundary $\partial\Omega = \Gamma$ (i.e. Γ given locally as graphs of Lipschitz functions in a finite number of appropriate cartesian coordinate systems, and Ω being locally on one side of Γ). Note that Γ may include corners but not cracks and cusps. Let $\Gamma_S \subset \Gamma$ denote the smooth part of Γ, i.e. excluding corners, edges, points of curvature jumps, etc. Let n denote the unit outward normal vector defined at Γ_S.

Let x_i $(i = 1,\dots,d)$ be a fixed cartesian coordinate system at the origin point O. Let $u = (u_1,\dots,u_d)$ be the displacement solution of the following BVP for the Navier equation with zero body forces:

$$c_{ijkl}u_{k,lj}(x) = c_{ijkl}\varepsilon_{kl,j}(u(x)) = 0, \qquad x \in \Omega, \quad (1a)$$

$$u_i(x) = g_i(x), \qquad x \in \Gamma_u, \quad (1b)$$

$$t_i(x) = (\mathscr{T}_{n(x)})_i(u(x)) = h_i(x), \qquad x \in \Gamma_t, \quad (1c)$$

with the fourth-order symmetric positively definite tensor of elastic stiffness c_{ijkl} $(i,j,k,l = 1,\dots,d)$, strain tensor ε_{ij}, traction operator $\mathscr{T}_n$ and the split of the boundary $\Gamma = \overline{\Gamma}_u \cup \overline{\Gamma}_t$ $(\emptyset = \Gamma_u \cap \Gamma_t)$ in accordance with the boundary conditions.

2.2 Elastic BIEs

The Somigliana displacement identity [Jaswon and Symm (1977); Baláš *et al.* (1989); París and Cañas (1997)] holds for the solution of the above BVP defined on a bounded homogenous Ω (interior BVP):

$$\begin{aligned}\chi_\Omega(x)u_i(x) = &\int_\Gamma U_{ij}(x,y)t_j(y)\mathrm{d}_y S \\ &- \int_\Gamma T_{ij}(x,y)u_j(y)\mathrm{d}_y S, \\ x \in \mathbb{R}^d \setminus \Gamma, &\quad i,j = 1,\dots,d,\end{aligned} \quad (2)$$

where χ_Ω is the characteristic function of Ω ($\chi_\Omega(x) = 1$ if $x \in \Omega$ and $\chi_\Omega(x) = 0$ if $x \notin \Omega \cup \Gamma$), U_{ij} is the fundamental solution in displacements of the Navier equation and T_{ij} represents the fundamental tractions, obtained from the fundamental solution via the traction operator: $T(x,y) = \left(\mathscr{T}_{n(y)}U(x,y)\right)^T$, T denoting the transpose matrix. Note that (2) is also valid for a solution of an exterior BVP defined on an unbounded Ω with a bounded Γ [Jaswon and Symm (1977); Baláš *et al.* (1989)] if the solution fulfills the well-known regularity condition at infinity:

$$\begin{aligned}&u_i(x) = U_{ij}(x,0)b_j + \mathrm{O}(\|x\|^{1-d}), \\ &\|x\| \to \infty, \; b_j = \int_\Gamma t_j(y)\mathrm{d}_y S.\end{aligned} \quad (3)$$

Applying the traction operator to (2) the Somigliana traction identity is obtained:

$$\begin{aligned}\chi_\Omega(x)t_i(x) = &\int_\Gamma T^*_{ij}(x,y)t_j(y)\mathrm{d}_y S \\ &- \int_\Gamma S_{ij}(x,y)u_j(y)\mathrm{d}_y S, \\ &x \in \mathbb{R}^d \setminus \Gamma,\end{aligned} \quad (4)$$

where $T^*(x,y) = \mathscr{T}_{n(x)}U(x,y)$, $S(x,y) = \mathscr{T}_{n(x)}T(x,y)$ and $n(x)$ is the unit vector normal to an auxiliary curve passing through the point x where the traction is to be evaluated.

With reference to the above defined integral kernels, let us recall the following reciprocity relations [Bonnet *et al.* (1998)]: $U(x,y) = U^T(y,x)$, $T^*(x,y) = T^T(y,x)$ and $S(x,y) = S^T(y,x)$. Additionally, the fundamental solution is symmetric, i.e. $U(x,y) = U^T(x,y)$, and, according to Mantič and París (1997a,b), also the hypersingular integral kernel S is symmetric in 2D, i.e. $S(x,y) = S^T(x,y)$. Additionally, the kernels $T^*(x,y)$ and $T(x,y)$ change their sign when evaluated using the normals defined with respect to the opposite sides of a curve.

After an asymptotic procedure applied to (2) and (4) for a boundary point $x \in \Gamma_S$, the following BIEs, sometimes called u-BIE and t-BIE respectively, are obtained [Baláš *et al.* (1989); Guiggiani *et al.* (1992); Guiggiani (1995); Mantič and París

(1995); Young (1996); París and Cañas (1997)]:

$$\frac{1}{2}u_i(x) = \int_\Gamma U_{ij}(x,y)t_j(y)\mathrm{d}_y S - \oint\!\!\!\!\!\!-_\Gamma T_{ij}(x,y)u_j(y)\mathrm{d}_y S, \quad (5a)$$

$$\frac{1}{2}t_i(x) = \oint\!\!\!\!\!\!-_\Gamma T^*_{ij}(x,y)t_j(y)\mathrm{d}_y S - \oint\!\!\!\!\!\!=_\Gamma S_{ij}(x,y)u_j(y)\mathrm{d}_y S, \quad (5b)$$

$$x \in \Gamma_S, \quad i,j = 1,\ldots,d.$$

the second and first integrals respectively on the right-hand sides of (5a) and (5b), with a strongly singular integral kernel, being evaluated in the sense of Cauchy principal value, and the second integral on the right-hand side of (5b), with a hypersingular integral kernel, being evaluated in the sense of Hadamard finite part.

Both aforementioned BIEs, (5a) and (5b), will be used in the following derivation of the SGBEM formulation for a DDBVP.

2.3 Domain decomposition

A DD approach starts with a split of Ω into several subdomains. For the sake of simplicity, a split into two non-overlapping subdomains Ω^A and Ω^B, whose respective boundaries are denoted as $\Gamma^A = \partial\Omega^A$ and $\Gamma^B = \partial\Omega^B$, will be considered hereinafter, Figure 1. The common part of Γ^A and Γ^B is denoted as $\Gamma_c = \Gamma^A \cap \Gamma^B$. Hence, reconsidering the boundary conditions (1b) and (1c) and the corresponding split of Γ, we can write $\Gamma^\eta = \overline{\Gamma}^\eta_u \cup \overline{\Gamma}^\eta_t \cup \overline{\Gamma}_c$, where $\eta = A,B$ and $\emptyset = \Gamma^\eta_u \cap \Gamma^\eta_t = \Gamma^\eta_u \cap \Gamma_c = \Gamma^\eta_t \cap \Gamma_c$.

The DDBVP for the Navier equation (1) can be written in the form:

$$c^\eta_{ijkl}u^\eta_{k,lj}(x) = c^\eta_{ijkl}\varepsilon_{kl,j}(u^\eta(x)) = 0, \quad x \in \Omega^\eta, \quad \eta = A,B, \quad (6a)$$

$$u^\eta_i(x) = g^\eta_i(x), \quad x \in \Gamma^\eta_u, \quad (6b)$$

$$t^\eta_i(x) = (\mathscr{T}_{n^\eta(x)})_i(u^\eta(x)) = h^\eta_i(x), \quad x \in \Gamma^\eta_t, \quad (6c)$$

$$u^A_i(x) = u^B_i(x), \quad x \in \Gamma_c, \quad (6d)$$

$$t^A_i(x) = -t^B_i(x), \quad x \in \Gamma_c, \quad (6e)$$

where the coupling conditions between Ω^A and Ω^B, equations (6d) and (6e) respectively, enforce compatibility of the displacements u^A and u^B defined on subdomains Ω^A and Ω^B and equilibrium of the tractions t^A and t^B defined on Γ^A and Γ^B. These coupling conditions will be formulated in a weak form in the variational formulation introduced in the next section.

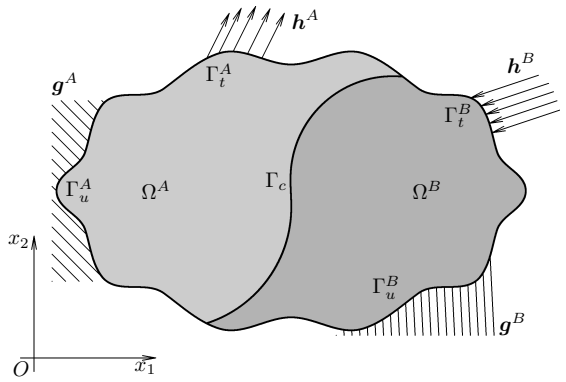

Figure 1: Domain decomposition problem.

3 Variational formulation

3.1 Energy functional for a DDBVP and its variation

Let us introduce an energy functional $E(u^A,u^B)$ as a function of displacements u^A and u^B. The functional E can be expressed in the following form:

$$E(u^A,u^B) = E^A_p(u^A) + E^B_p(u^B) + E_c(u^A,u^B), \quad (7)$$

where the functionals $E^A_p(u^A)$ and $E^B_p(u^B)$ represent the total energy functionals [Hartmann (1985)] associated to Ω^A and Ω^B, respectively, without the parts belonging to Γ_c. These functionals can be expressed in the form:

$$E^\eta_p(u^\eta) = \frac{1}{2}\int_{\Omega^\eta} \varepsilon_{ij}(u^\eta)c^\eta_{ijkl}\varepsilon_{kl}(u^\eta)\mathrm{d}V - \int_{\Gamma^\eta_t} h^\eta_i\, u^\eta_i \mathrm{d}S - \int_{\Gamma^\eta_u} t^\eta_i\,(u^\eta_i - g^\eta_i)\,\mathrm{d}S, \quad \eta = A,B, \quad (8)$$

where the fufnctions t^η represent the tractions of the displacement solutions u^η calculated via the traction operator $\mathscr{T}_n$, i. e. $t^\eta = \mathscr{T}_{n^\eta}(u^\eta)$.

The last term in (7), which defines a form of interface energy associated to coupling conditions

across Γ_c, takes the form:

$$E_c(u^A,u^B) = -\int_{\Gamma_c} t_i^A \left(u_i^A - u_i^B\right) \mathrm{d}S, \tag{9}$$

which indicates that the solution of the DDBVP will cause this term, called interface constraint functional, to vanish.

The condition of the critical point of the functional E in (7) means that the first order variation of E vanishes, which can be written after a rearrangement as:

$$0 = \delta E(u^A,u^B;\delta u^A,\delta u^B) \tag{10a}$$

$$= \left(\int_{\Omega^A} \varepsilon_{ij}(\delta u^A) c_{ijkl}^A \varepsilon_{kl}(u^A)\mathrm{d}V - \int_{\Gamma_t^A} h_i^A\, \delta u_i^A \mathrm{d}S - \int_{\Gamma_u^A} t_i^A\, \delta u_i^A \mathrm{d}S - \int_{\Gamma_c} t_i^A\, \delta u_i^A \mathrm{d}S\right) \tag{10b}$$

$$+ \left(\int_{\Omega^B} \varepsilon_{ij}(\delta u^B) c_{ijkl}^B \varepsilon_{kl}(u^B)\mathrm{d}V - \int_{\Gamma_t^B} h_i^B\, \delta u_i^B \mathrm{d}S - \int_{\Gamma_u^B} t_i^B\, \delta u_i^B \mathrm{d}S - \int_{\Gamma_c} t_i^B\, \delta u_i^B \mathrm{d}S\right) \tag{10c}$$

$$- \left(\int_{\Gamma_u^A} \delta t_i^A \left(u_i^A - g_i^A\right) \mathrm{d}S + \int_{\Gamma_u^B} \delta t_i^B \left(u_i^B - g_i^B\right) \mathrm{d}S\right) \tag{10d}$$

$$- \left(\int_{\Gamma_c} \delta t_i^A \left(u_i^A - u_i^B\right) \mathrm{d}S - \int_{\Gamma_c} \delta u_i^B \left(t_i^A + t_i^B\right) \mathrm{d}S\right). \tag{10e}$$

As will be explained in what follows, relation (10) implies that the solution of the DDBVP (6) is the critical point of the functional E. If the volume integrals in expressions (10b) and (10c) are integrated by parts, giving the volume integrals with the virtual displacements δu^η without derivatives, these expressions render the Navier equations (6a) for functions u^A and u^B and the boundary conditions for tractions (6c). Expressions (10d) vanish only if the boundary conditions for displacements (6b) are fulfilled.

Finally, the line (10e) enforces the equilibrium (6e) and compatibility (6d) conditions at Γ_c in a weak sense: *the compatibility is imposed through the displacement (Dirichlet) boundary conditions on subdomain Ω^A along Γ_c with 'prescribed' displacements u^B, and the equilibrium is imposed through the traction (Neumann) boundary conditions on subdomain Ω^B along Γ_c with 'prescribed' tractions t^A.*

The relations between the functions defined along the boundary Γ_c are schematically presented in Figure 2. An arrow connects two functions which are equal to each other in the weak sense due to the relation whose number is written in the parentheses close to the arrow. We conclude that finding the critical point of the energy functional E (7) is equivalent to solving the DDBVP (6).

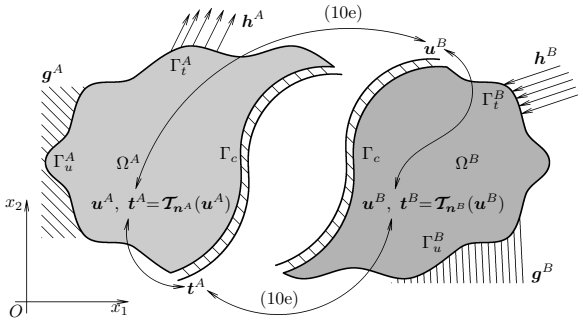

Figure 2: Explanation of the variables in the functional E.

In order to obtain a relation suitable for an SGBEM approach, equation (10) is modified integrating by parts the volume integrals, but now yielding displacements u^η without derivatives. Recalling the meaning of δt^η as $\delta t^\eta = \mathscr{T}_{n^\eta}(\delta u^\eta)$, the following relation is obtained:

$$\begin{aligned} 0 = &\left(-\int_{\Omega^A} \frac{\partial}{\partial x_l}\left(\varepsilon_{ij}(\delta u^A) c_{ijkl}^A\right) u_k^A \mathrm{d}V \right.\\ &+ \int_{\Gamma_t^A} u_i^A\, \delta t_i^A \mathrm{d}S + \int_{\Gamma_u^A} g_i^A\, \delta t_i^A \mathrm{d}S + \int_{\Gamma_c} u_i^A\, \delta t_i^A \mathrm{d}S\\ &\left. - \int_{\Gamma_t^A} h_i^A\, \delta u_i^A \mathrm{d}S - \int_{\Gamma_u^A} t_i^A\, \delta u_i^A \mathrm{d}S - \int_{\Gamma_c} t_i^A\, \delta u_i^A \mathrm{d}S\right)\\ &+ \left(-\int_{\Omega^B} \frac{\partial}{\partial x_l}\left(\varepsilon_{ij}(\delta u^B) c_{ijkl}^B\right) u_k^B \mathrm{d}V \right.\\ &+ \int_{\Gamma_t^B} u_i^B\, \delta t_i^B \mathrm{d}S + \int_{\Gamma_u^B} g_i^B\, \delta t_i^B \mathrm{d}S + \int_{\Gamma_c} u_i^B\, \delta t_i^B \mathrm{d}S\\ &\left. - \int_{\Gamma_t^B} h_i^B\, \delta u_i^B \mathrm{d}S - \int_{\Gamma_u^B} t_i^B\, \delta u_i^B \mathrm{d}S - \int_{\Gamma_c} t_i^B\, \delta u_i^B \mathrm{d}S\right)\\ &- \left(\int_{\Gamma_c} \delta t_i^A \left(u_i^A - u_i^B\right) \mathrm{d}S - \int_{\Gamma_c} \delta u_i^B \left(t_i^A + t_i^B\right) \mathrm{d}S\right). \end{aligned} \tag{11}$$

3.2 Symmetric variational formulation of BIEs for a DDBVP

So far, no restrictions on the virtual displacements δu^η have been set. Let us consider only those δu^η which satisfy the Navier equation in Ω^η, causing the volume integrals in (11) to vanish. Then, these displacements have the following boundary integral representation:

$$\begin{aligned}\delta u_i^\eta(x) = &\int_{\Gamma^\eta} U_{ij}^\eta(x,y)\varphi_j^\eta(y)\mathrm{d}_y S \\ &- \int_{\Gamma^\eta} T_{ij}^\eta(x,y)\psi_j^\eta(y)\mathrm{d}_y S, \\ &x\in\Omega^\eta,\end{aligned} \tag{12}$$

where the functions φ^η and ψ^η can be considered to have the form:

$$\varphi^\eta = \delta t^\eta - \delta\tilde{t}^\eta, \qquad \psi^\eta = \delta u^\eta - \delta\tilde{u}^\eta. \tag{13}$$

Note that the representation formula (12) can be obtained from the Somigliana identity (2) written for Ω^η and for each connected subset of its complement in $\mathbb{R}^d$. In fact, the function $\delta\tilde{u}^\eta$ represents the trace of a displacement solution of the Navier equation at each such connected subset, equipped with the radiation condition (3) if the pertinent subset is unbounded, and $\delta\tilde{t}^\eta$ represents the corresponding tractions. The boundary conditions for these functions can be chosen arbitrarily. They are chosen here satisfying the following conditions:

$$\begin{aligned}&\varphi^\eta(x) = 0, \quad x\in\Gamma_t^\eta, \quad \eta = A,B, \\ &\varphi^A(x) = \delta t^A(x), \quad x\in\Gamma_c,\end{aligned} \tag{14a}$$

$$\begin{aligned}&\psi^\eta(x) = 0, \quad x\in\Gamma_u^\eta, \quad \eta = A,B, \\ &\psi^B(x) = \delta u^B(x), \quad x\in\Gamma_c,\end{aligned} \tag{14b}$$

so that the boundary conditions for $\delta\tilde{t}^\eta$ and $\delta\tilde{u}^\eta$ read:

$$\begin{aligned}&\delta\tilde{t}^\eta(x) = \delta t^\eta(x), \quad x\in\Gamma_t^\eta, \quad \eta = A,B, \\ &\delta\tilde{t}^A(x) = 0, \quad x\in\Gamma_c,\end{aligned} \tag{15a}$$

$$\begin{aligned}&\delta\tilde{u}^\eta(x) = \delta u^\eta(x), \quad x\in\Gamma_u^\eta, \quad \eta = A,B, \\ &\delta\tilde{u}^B(x) = 0, \quad x\in\Gamma_c.\end{aligned} \tag{15b}$$

The integral representation (12) can be written with this particular choice of the functions φ^η and ψ^η in the form:

$$\begin{aligned}\delta u_i^\eta(x) = &\int_{\Gamma_u^\eta} U_{ij}^\eta(x,y)\varphi_j^\eta(y)\mathrm{d}_y S \\ &- \int_{\Gamma_t^\eta} T_{ij}^\eta(x,y)\psi_j^\eta(y)\mathrm{d}_y S \\ &+ \int_{\Gamma_c} U_{ij}^\eta(x,y)\varphi_j^\eta(y)\mathrm{d}_y S \\ &- \int_{\Gamma_c} T_{ij}^\eta(x,y)\psi_j^\eta(y)\mathrm{d}_y S, \\ &x\in\Omega^\eta,\end{aligned} \tag{16}$$

which for the limit $x\to x'\in\Gamma^\eta$ (or directly utilizing the pertinent difference of equations (5a) for Ω^η and the connected subsets of its complement in $\mathbb{R}^d$) renders the relations:

$$\begin{aligned}\delta u_i^\eta(x') = &\int_{\Gamma_u^\eta} U_{ij}^\eta(x',y)\varphi_j^\eta(y)\mathrm{d}_y S \\ &- \int_{\Gamma_t^\eta} T_{ij}^\eta(x',y)\psi_j^\eta(y)\mathrm{d}_y S \\ &+ \int_{\Gamma_c} U_{ij}^\eta(x',y)\varphi_j^\eta(y)\mathrm{d}_y S \\ &- \int_{\Gamma_c} T_{ij}^\eta(x',y)\psi_j^\eta(y)\mathrm{d}_y S, \\ &x'\in\Gamma_u^\eta,\end{aligned} \tag{17a}$$

$$\begin{aligned}\delta u_i^\eta(x') = &\int_{\Gamma_u^\eta} U_{ij}^\eta(x',y)\varphi_j^\eta(y)\mathrm{d}_y S \\ &- \left(-\frac{1}{2}\psi_i^\eta(x') + \oint_{\Gamma_t^\eta} T_{ij}^\eta(x',y)\psi_j^\eta(y)\mathrm{d}_y S\right) \\ &+ \int_{\Gamma_c} U_{ij}^\eta(x',y)\varphi_j^\eta(y)\mathrm{d}_y S \\ &- \int_{\Gamma_c} T_{ij}^\eta(x',y)\psi_j^\eta(y)\mathrm{d}_y S, \\ &x'\in(\Gamma_t^\eta)_S,\end{aligned} \tag{17b}$$

$$\begin{aligned}\delta u_i^\eta(x') = &\int_{\Gamma_u^\eta} U_{ij}^\eta(x',y)\varphi_j^\eta(y)\mathrm{d}_y S \\ &- \int_{\Gamma_t^\eta} T_{ij}^\eta(x',y)\psi_j^\eta(y)\mathrm{d}_y S \\ &+ \int_{\Gamma_c} U_{ij}^\eta(x',y)\varphi_j^\eta(y)\mathrm{d}_y S \\ &- \left(-\frac{1}{2}\psi_i^\eta(x') + \oint_{\Gamma_c} T_{ij}^\eta(x',y)\psi_j^\eta(y)\mathrm{d}_y S\right), \\ &x'\in(\Gamma_c)_S.\end{aligned} \tag{17c}$$

Analogously, the boundary integral representation of the virtual tractions δt^η (see also equation (5b))

can be obtained:

$$\begin{aligned}\delta t_i^\eta(x') = &\left(\frac{1}{2}\varphi_i^\eta(x') + \oint_{\Gamma_u^\eta} T_{ij}^{\eta *}(x',y)\varphi_j^\eta(y)\mathrm{d}_y S\right)\\ &- \int_{\Gamma_t^\eta} S_{ij}^\eta(x',y)\psi_j^\eta(y)\mathrm{d}_y S\\ &+ \int_{\Gamma_c} T_{ij}^{\eta *}(x',y)\varphi_j^\eta(y)\mathrm{d}_y S\\ &- \int_{\Gamma_c} S_{ij}^\eta(x',y)\psi_j^\eta(y)\mathrm{d}_y S,\\ &x' \in (\Gamma_u^\eta)_S,\end{aligned} \tag{18a}$$

$$\begin{aligned}\delta t_i^\eta(x') = &\int_{\Gamma_u^\eta} T_{ij}^{\eta *}(x',y)\varphi_j^\eta(y)\mathrm{d}_y S\\ &- \oint_{\Gamma_t^\eta} S_{ij}^\eta(x',y)\psi_j^\eta(y)\mathrm{d}_y S\\ &+ \int_{\Gamma_c} T_{ij}^{\eta *}(x',y)\varphi_j^\eta(y)\mathrm{d}_y S\\ &- \int_{\Gamma_c} S_{ij}^\eta(x',y)\psi_j^\eta(y)\mathrm{d}_y S,\\ &x' \in (\Gamma_t^\eta)_S,\end{aligned} \tag{18b}$$

$$\begin{aligned}\delta t_i^\eta(x') = &\int_{\Gamma_u^\eta} T_{ij}^{\eta *}(x',y)\varphi_j^\eta(y)\mathrm{d}_y S\\ &- \int_{\Gamma_t^\eta} S_{ij}^\eta(x',y)\psi_j^\eta(y)\mathrm{d}_y S\\ &+ \left(\frac{1}{2}\varphi_i^\eta(x') + \oint_{\Gamma_c} T_{ij}^{\eta *}(x',y)\varphi_j^\eta(y)\mathrm{d}_y S\right)\\ &- \oint_{\Gamma_c} S_{ij}^\eta(x',y)\psi_j^\eta(y)\mathrm{d}_y S,\\ &x' \in (\Gamma_c)_S.\end{aligned} \tag{18c}$$

Let the representations (17) and (18) be substituted into (11). Recall that the volume integrals in (11) vanish and the variations δt^A and δu^B along Γ_c are equal to φ^A and ψ^B, respectively, due to (14). Hence,

$$\begin{aligned}0 = &\int_{\Gamma_t^A} u_i^A(x)\left(\int_{\Gamma_u^A} T_{ij}^{A*}(x,y)\varphi_j^A(y)\mathrm{d}_y S\right.\\ &- \oint_{\Gamma_t^A} S_{ij}^A(x,y)\psi_j^A(y)\mathrm{d}_y S + \int_{\Gamma_c} T_{ij}^{A*}(x,y)\varphi_j^A(y)\mathrm{d}_y S\\ &\left.- \int_{\Gamma_c} S_{ij}^A(x,y)\psi_j^A(y)\mathrm{d}_y S\right)\mathrm{d}_x S\\ &+ \int_{\Gamma_u^A} g_i^A(x)\left(\left(\frac{1}{2}\varphi_i^A(x) + \oint_{\Gamma_u^A} T_{ij}^{A*}(x,y)\varphi_j^A(y)\mathrm{d}_y S\right)\right.\\ &- \int_{\Gamma_t^A} S_{ij}^A(x,y)\psi_j^A(y)\mathrm{d}_y S + \int_{\Gamma_c} T_{ij}^{A*}(x,y)\varphi_j^A(y)\mathrm{d}_y S\\ &\left.- \int_{\Gamma_c} S_{ij}^A(x,y)\psi_j^A(y)\mathrm{d}_y S\right)\mathrm{d}_x S\\ &+ \int_{\Gamma_c} u_i^A(x)\left(\int_{\Gamma_u^A} T_{ij}^{A*}(x,y)\varphi_j^A(y)\mathrm{d}_y S\right.\\ &- \int_{\Gamma_t^A} S_{ij}^A(x,y)\psi_j^A(y)\mathrm{d}_y S\\ &+ \left(\frac{1}{2}\varphi_i^A(x) + \oint_{\Gamma_c} T_{ij}^{A*}(x,y)\varphi_j^A(y)\mathrm{d}_y S\right)\\ &\left.- \oint_{\Gamma_c} S_{ij}^A(x,y)\psi_j^A(y)\mathrm{d}_y S\right)\mathrm{d}_x S\\ &- \int_{\Gamma_t^A} h_i^A(x)\left(\int_{\Gamma_u^A} U_{ij}^A(x,y)\varphi_j^A(y)\mathrm{d}_y S\right.\\ &- \left(-\frac{1}{2}\psi_i^A(x) + \oint_{\Gamma_t^A} T_{ij}^A(x,y)\psi_j^A(y)\mathrm{d}_y S\right)\\ &+ \int_{\Gamma_c} U_{ij}^A(x,y)\varphi_j^A(y)\mathrm{d}_y S\\ &\left.- \int_{\Gamma_c} T_{ij}^A(x,y)\psi_j^A(y)\mathrm{d}_y S\right)\mathrm{d}_x S\\ &- \int_{\Gamma_u^A} t_i^A(x)\left(\int_{\Gamma_u^A} U_{ij}^A(x,y)\varphi_j^A(y)\mathrm{d}_y S\right.\\ &- \int_{\Gamma_t^A} T_{ij}^A(x,y)\psi_j^A(y)\mathrm{d}_y S + \int_{\Gamma_c} U_{ij}^A(x,y)\varphi_j^A(y)\mathrm{d}_y S\\ &\left.- \int_{\Gamma_c} T_{ij}^A(x,y)\psi_j^A(y)\mathrm{d}_y S\right)\mathrm{d}_x S\\ &- \int_{\Gamma_c} t_i^A(x)\left(\int_{\Gamma_u^A} U_{ij}^A(x,y)\varphi_j^A(y)\mathrm{d}_y S\right.\\ &- \int_{\Gamma_t^A} T_{ij}^A(x,y)\psi_j^A(y)\mathrm{d}_y S + \int_{\Gamma_c} U_{ij}^A(x,y)\varphi_j^A(y)\mathrm{d}_y S\\ &\left.- \left(-\frac{1}{2}\psi_i^A(x) + \oint_{\Gamma_c} T_{ij}^A(x,y)\psi_j^A(y)\mathrm{d}_y S\right)\right)\mathrm{d}_x S\\ &+ \int_{\Gamma_t^B} u_i^B(x)\left(\int_{\Gamma_u^B} T_{ij}^{B*}(x,y)\varphi_j^B(y)\mathrm{d}_y S\right.\\ &- \oint_{\Gamma_t^B} S_{ij}^B(x,y)\psi_j^B(y)\mathrm{d}_y S + \int_{\Gamma_c} T_{ij}^{B*}(x,y)\varphi_j^B(y)\mathrm{d}_y S\\ &\left.- \int_{\Gamma_c} S_{ij}^B(x,y)\psi_j^B(y)\mathrm{d}_y S\right)\mathrm{d}_x S\\ &+ \int_{\Gamma_u^B} g_i^B(x)\left(\left(\frac{1}{2}\varphi_i^B(x) + \oint_{\Gamma_u^B} T_{ij}^{B*}(x,y)\varphi_j^B(y)\mathrm{d}_y S\right)\right.\\ &- \int_{\Gamma_t^B} S_{ij}^B(x,y)\psi_j^B(y)\mathrm{d}_y S + \int_{\Gamma_c} T_{ij}^{B*}(x,y)\varphi_j^B(y)\mathrm{d}_y S\\ &\left.- \int_{\Gamma_c} S_{ij}^B(x,y)\psi_j^B(y)\mathrm{d}_y S\right)\mathrm{d}_x S\\ &+ \int_{\Gamma_c} u_i^B(x)\left(\int_{\Gamma_u^B} T_{ij}^{B*}(x,y)\varphi_j^B(y)\mathrm{d}_y S\right.\\ &- \int_{\Gamma_t^B} S_{ij}^B(x,y)\psi_j^B(y)\mathrm{d}_y S\\ &\left.+ \left(\frac{1}{2}\varphi_i^B(x) + \oint_{\Gamma_c} T_{ij}^{B*}(x,y)\varphi_j^B(y)\mathrm{d}_y S\right)\right.\end{aligned}$$

$$
\begin{aligned}
&-\oint\!\!\!\!\!\!-_{\Gamma_c} S_{ij}^B(x,y)\psi_j^B(y)\mathrm{d}_y S\Big)\,\mathrm{d}_x S\\
&-\int_{\Gamma_t^B} h_i^B(x)\left(\int_{\Gamma_u^B} U_{ij}^B(x,y)\varphi_j^B(y)\mathrm{d}_y S\right.\\
&-\left(-\frac{1}{2}\psi_i^B(x)+\oint\!\!\!\!\!\!-_{\Gamma_t^B} T_{ij}^B(x,y)\psi_j^B(y)\mathrm{d}_y S\right)\\
&+\int_{\Gamma_c} U_{ij}^B(x,y)\varphi_j^B(y)\mathrm{d}_y S\\
&\left.-\int_{\Gamma_c} T_{ij}^B(x,y)\psi_j^B(y)\mathrm{d}_y S\right)\mathrm{d}_x S\\
&-\int_{\Gamma_u^B} t_i^B(x)\left(\int_{\Gamma_u^B} U_{ij}^B(x,y)\varphi_j^B(y)\mathrm{d}_y S\right.\\
&-\int_{\Gamma_t^B} T_{ij}^B(x,y)\psi_j^B(y)\mathrm{d}_y S+\int_{\Gamma_c} U_{ij}^B(x,y)\varphi_j^B(y)\mathrm{d}_y S\\
&\left.-\int_{\Gamma_c} T_{ij}^B(x,y)\psi_j^B(y)\mathrm{d}_y S\right)\mathrm{d}_x S\\
&-\int_{\Gamma_c} t_i^B(x)\left(\int_{\Gamma_u^B} U_{ij}^B(x,y)\varphi_j^B(y)\mathrm{d}_y S\right.\\
&-\int_{\Gamma_t^B} T_{ij}^B(x,y)\psi_j^B(y)\mathrm{d}_y S+\int_{\Gamma_c} U_{ij}^B(x,y)\varphi_j^B(y)\mathrm{d}_y S\\
&\left.-\left(-\frac{1}{2}\psi_i^B(x)+\oint\!\!\!\!\!\!-_{\Gamma_c} T_{ij}^B(x,y)\psi_j^B(y)\mathrm{d}_y S\right)\right)\mathrm{d}_x S\\
&-\int_{\Gamma_c}\varphi_i^A(y)\,\left(u_i^A(y)-u_i^B(y)\right)\mathrm{d}_y S\\
&+\int_{\Gamma_c}\psi_i^B(y)\,\left(t_i^A(y)+t_i^B(y)\right)\mathrm{d}_y S.
\end{aligned}
\tag{19}
$$

Finally, to obtain a variational formulation of the BIE system for SGBEM solution of DDBVPs, first the order of the integration in the double integrals is interchanged, and then the terms in the expression obtained are reordered to gather together the terms with the same function φ^η or ψ^η, utilizing the above mentioned reciprocity properties of the integral operators. The interchangeability of the order of the Cauchy principal value and Hadamard finite part integrals with the common integral has been assumed due to the results of the analysis presented in Bonnet (1995). Hence,

$$
\begin{aligned}
0=&\int_{\Gamma_u^A}\varphi_j^A(y)\left(-\int_{\Gamma_u^A} U_{ji}^A(y,x)t_i^A(x)\mathrm{d}_x S\right.\\
&+\int_{\Gamma_t^A} T_{ji}^A(y,x)u_i^A(x)\mathrm{d}_x S-\int_{\Gamma_c} U_{ji}^A(y,x)t_i^A(x)\mathrm{d}_x S\\
&+\int_{\Gamma_c} T_{ji}^A(y,x)u_i^A(x)\mathrm{d}_x S-\int_{\Gamma_t^A} U_{ji}^A(y,x)h_i^A(x)\mathrm{d}_x S\\
&\left.+\left(\frac{1}{2}g_j^A(y)+\oint\!\!\!\!\!\!-_{\Gamma_u^A} T_{ji}^A(y,x)g_i^A(x)\mathrm{d}_x S\right)\right)\mathrm{d}_y S\\
&+\int_{\Gamma_t^A}\psi_j^A(y)\left(\int_{\Gamma_u^A} T_{ji}^{A*}(y,x)t_i^A(x)\mathrm{d}_x S\right.\\
&-\oint\!\!\!\!\!\!-_{\Gamma_t^A} S_{ji}^A(y,x)u_i^A(x)\mathrm{d}_x S+\int_{\Gamma_c} T_{ji}^{A*}(y,x)t_i^A(x)\mathrm{d}_x S\\
&-\int_{\Gamma_c} S_{ji}^A(y,x)u_i^A(x)\mathrm{d}_x S\\
&+\left(-\frac{1}{2}h_j^A(y)+\oint\!\!\!\!\!\!-_{\Gamma_t^A} T_{ji}^{A*}(y,x)h_i^A(x)\mathrm{d}_x S\right)\\
&\left.-\int_{\Gamma_u^A} S_{ji}^A(y,x)g_i^A(x)\mathrm{d}_x S\right)\mathrm{d}_y S\\
&+\int_{\Gamma_c}\varphi_j^A(y)\left(u_j^B(y)-\int_{\Gamma_u^A} U_{ji}^A(y,x)t_i^A(x)\mathrm{d}_x S\right.\\
&+\int_{\Gamma_t^A} T_{ji}^A(y,x)u_i^A(x)\mathrm{d}_x S-\int_{\Gamma_c} U_{ji}^A(y,x)t_i^A(x)\mathrm{d}_x S\\
&+\left(-\frac{1}{2}u_j^A(y)+\oint\!\!\!\!\!\!-_{\Gamma_c} T_{ji}^A(y,x)u_i^A(x)\mathrm{d}_x S\right)\\
&\left.-\int_{\Gamma_t^A} U_{ji}^A(y,x)h_i^A(x)\mathrm{d}_x S+\int_{\Gamma_u^A} T_{ji}^A(y,x)g_i^A(x)\mathrm{d}_x S\right)\mathrm{d}_y S\\
&+\int_{\Gamma_c}\psi_j^A(y)\left(\int_{\Gamma_u^A} T_{ji}^{A*}(y,x)t_i^A(x)\mathrm{d}_x S\right.\\
&-\int_{\Gamma_t^A} S_{ji}^A(y,x)u_i^A(x)\mathrm{d}_x S\\
&+\left(-\frac{1}{2}t_j^A(y)+\oint\!\!\!\!\!\!-_{\Gamma_c} T_{ji}^{A*}(y,x)t_i^A(x)\mathrm{d}_x S\right)\\
&-\oint\!\!\!\!\!\!-_{\Gamma_c} S_{ji}^A(y,x)u_i^A(x)\mathrm{d}_x S+\int_{\Gamma_t^A} T_{ji}^{A*}(y,x)h_i^A(x)\mathrm{d}_x S\\
&\left.-\int_{\Gamma_u^A} S_{ji}^A(y,x)g_i^A(x)\mathrm{d}_x S\right)\mathrm{d}_y S\\
&+\int_{\Gamma_u^B}\varphi_j^B(y)\left(-\int_{\Gamma_u^B} U_{ji}^B(y,x)t_i^B(x)\mathrm{d}_x S\right.\\
&+\int_{\Gamma_t^B} T_{ji}^B(y,x)u_i^B(x)\mathrm{d}_x S-\int_{\Gamma_c} U_{ji}^B(y,x)t_i^B(x)\mathrm{d}_x S\\
&+\int_{\Gamma_c} T_{ji}^B(y,x)u_i^B(x)\mathrm{d}_x S-\int_{\Gamma_t^B} U_{ji}^B(y,x)h_i^B(x)\mathrm{d}_x S\\
&\left.+\left(\frac{1}{2}g_j^B(y)+\oint\!\!\!\!\!\!-_{\Gamma_u^B} T_{ji}^B(y,x)g_i^B(x)\mathrm{d}_x S\right)\right)\mathrm{d}_y S\\
&+\int_{\Gamma_t^B}\psi_j^B(y)\left(\int_{\Gamma_u^B} T_{ji}^{B*}(y,x)t_i^B(x)\mathrm{d}_x S\right.\\
&-\oint\!\!\!\!\!\!-_{\Gamma_t^B} S_{ji}^B(y,x)u_i^B(x)\mathrm{d}_x S+\int_{\Gamma_c} T_{ji}^{B*}(y,x)t_i^B(x)\mathrm{d}_x S\\
&-\int_{\Gamma_c} S_{ji}^B(y,x)u_i^B(x)\mathrm{d}_x S\\
&+\left(-\frac{1}{2}h_j^B(y)+\oint\!\!\!\!\!\!-_{\Gamma_t^B} T_{ji}^{B*}(y,x)h_i^B(x)\mathrm{d}_x S\right)\\
&\left.-\int_{\Gamma_u^B} S_{ji}^B(y,x)g_i^B(x)\mathrm{d}_x S\right)\mathrm{d}_y S\\
&+\int_{\Gamma_c}\varphi_j^B(y)\left(-\int_{\Gamma_u^B} U_{ji}^B(y,x)t_i^B(x)\mathrm{d}_x S\right.
\end{aligned}
$$

$$
\begin{aligned}
&+\int_{\Gamma_t^B} T_{ji}^B(y,x)u_i^B(x)\mathrm{d}_x S-\int_{\Gamma_c} U_{ji}^B(y,x)t_i^B(x)\mathrm{d}_x S\\
&+\left(\frac{1}{2}u_j^B(y)+\oint_{\Gamma_c} T_{ji}^B(y,x)u_i^B(x)\mathrm{d}_x S\right)\\
&-\int_{\Gamma_t^B} U_{ji}^B(y,x)h_i^B(x)\mathrm{d}_x S\\
&+\int_{\Gamma_u^B} T_{ji}^B(y,x)g_i^B(x)\mathrm{d}_x S\Big)\,\mathrm{d}_y S\\
&+\int_{\Gamma_c}\psi_j^B(y)\left(t_j^A(y)+\int_{\Gamma_u^B} T_{ji}^{B*}(y,x)t_i^B(x)\mathrm{d}_x S\right.\\
&-\int_{\Gamma_t^B} S_{ji}^B(y,x)u_i^B(x)\mathrm{d}_x S\\
&+\left(\frac{1}{2}t_j^B(y)+\oint_{\Gamma_c} T_{ji}^{B*}(y,x)t_i^B(x)\mathrm{d}_x S\right)\\
&-\oint_{\Gamma_c} S_{ji}^B(y,x)u_i^B(x)\mathrm{d}_x S+\int_{\Gamma_t^B} T_{ji}^{B*}(y,x)h_i^B(x)\mathrm{d}_x S\\
&\left.-\int_{\Gamma_u^B} S_{ji}^B(y,x)g_i^B(x)\mathrm{d}_x S\right)\mathrm{d}_y S.
\end{aligned}
\tag{20}
$$

Introducing the following operator notation will allow us to rewrite the variational formulation of the BIE system (20) in a compact and transparent form. Let

$$
\omega_r^{\eta T} Z_{rs}^{\eta} w_s^{\eta}=\int_{\Gamma_r^{\eta}}\omega_j^{\eta}(y)\left(\int_{\Gamma_s^{\eta}} Z_{ji}^{\eta}(y,x)w_i^{\eta}(x)\mathrm{d}_x S\right)\mathrm{d}_y S,
\tag{21}
$$

where ω stands for φ or ψ, w stands for u or t, r and s stand for u, t or c, and Z stands for U, T, T^* or S, and where the inner integral can be regular, weakly singular, Cauchy principal value or Hadamard finite part integral. Hereinafter, $u_r^{\eta}=u^{\eta}|_{\Gamma_r^{\eta}}$ and $t_r^{\eta}=t^{\eta}|_{\Gamma_r^{\eta}}$ for $r=u,t$ and $u_c^{\eta}=u^{\eta}|_{\Gamma_c}$ and $t_c^{\eta}=t^{\eta}|_{\Gamma_c}$ for $\eta=A,B$ mean the restrictions of displacements and tractions on the respective boundary parts. Then (20) reads:

$$
\begin{aligned}
0=&\varphi_u^{AT}\left(-U_{uu}^A t_u^A+T_{ut}^A u_t^A-U_{uc}^A t_c^A+T_{uc}^A u_c^A\right.\\
&\left.-U_{ut}^A h^A+\left(\frac{1}{2}I_{uu}^A+T_{uu}^A\right)g^A\right)\\
&+\psi_t^{AT}\left(T_{tu}^{A*}t_u^A-S_{tt}^A u_t^A+T_{tc}^{A*}t_c^A-S_{tc}^A u_c^A\right.\\
&\left.+\left(-\frac{1}{2}I_{tt}^A+T_{tt}^{A*}\right)h^A-S_{uu}^A g^A\right)\\
&+\varphi_c^{AT}\left(-U_{cu}^A t_u^A+T_{ct}^A u_t^A-U_{cc}^A t_c^A\right.\\
&\left.+\left(-\frac{1}{2}I_{cc}^A+T_{cc}^A\right)u_c^A\right.\\
&\left.+I_{cc}^{AB}u_c^B-U_{ct}^A h^A+T_{cu}^A g^A\right)\\
&+\psi_c^{AT}\left(T_{cu}^{A*}t_u^A-S_{ct}^A u_t^A+\left(-\frac{1}{2}I_{cc}^A+T_{cc}^{A*}\right)t_c^A\right.\\
&\left.-S_{cc}^A u_c^A+T_{ct}^{A*}h^A-S_{cu}^A g^A\right)\\
&+\varphi_u^{BT}\left(-U_{uu}^B t_u^B+T_{ut}^B u_t^B-U_{uc}^B t_c^B+T_{uc}^B u_c^B\right.\\
&\left.-U_{ut}^B h^B+\left(\frac{1}{2}I_{uu}^B+T_{uu}^B\right)g^B\right)\\
&+\psi_t^{BT}\left(T_{tu}^{B*}t_u^B-S_{tt}^B u_t^B+T_{tc}^{B*}t_c^B-S_{tc}^B u_c^B\right.\\
&\left.+\left(-\frac{1}{2}I_{tt}^B+T_{tt}^{B*}\right)h^B-S_{uu}^B g^B\right)\\
&+\varphi_c^{BT}\left(-U_{cu}^B t_u^B+T_{ct}^B u_t^B-U_{cc}^B t_c^B\right.\\
&\left.+\left(\frac{1}{2}I_{cc}^B+T_{cc}^B\right)u_c^B-U_{ct}^B h^B+T_{cu}^B g^B\right)\\
&+\psi_c^{BT}\left(T_{cu}^{B*}t_u^B-S_{ct}^B u_t^B+\left(\frac{1}{2}I_{cc}^B+T_{cc}^{B*}\right)t_c^B\right.\\
&\left.-S_{cc}^B u_c^B+I_{cc}^{BA}t_c^A+T_{ct}^{B*}h^B-S_{cu}^B g^B\right)
\end{aligned}
\tag{22}
$$

or equivalently in matrix-operator form:

$$
\begin{aligned}
&\begin{pmatrix}\varphi_u^A\\ \psi_t^A\\ \varphi_c^A\\ \psi_c^A\\ \varphi_u^B\\ \psi_t^B\\ \varphi_c^B\\ \psi_c^B\end{pmatrix}^T
\begin{pmatrix} MATRIX \\ I \end{pmatrix}
\begin{pmatrix}t_u^A\\ u_t^A\\ t_c^A\\ u_c^A\\ t_u^B\\ u_t^B\\ t_c^B\\ u_c^B\end{pmatrix}\\
&=\begin{pmatrix}\varphi_u^A\\ \psi_t^A\\ \varphi_c^A\\ \psi_c^A\\ \varphi_u^B\\ \psi_t^B\\ \varphi_c^B\\ \psi_c^B\end{pmatrix}^T
\begin{pmatrix} MATRIX \\ II \end{pmatrix}
\begin{pmatrix}h^A\\ g^A\\ h^B\\ g^B\end{pmatrix},
\end{aligned}
\tag{23}
$$

where

$$\begin{pmatrix} MATRIX \\ I \end{pmatrix} = \begin{pmatrix} -U^A_{uu} & T^A_{ut} & -U^A_{uc} & T^A_{uc} & 0 & 0 & 0 & 0 \\ T^{A*}_{tu} & -S^A_{tt} & T^{A*}_{tc} & -S^A_{tc} & 0 & 0 & 0 & 0 \\ -U^A_{cu} & T^A_{ct} & -U^A_{cc} & -\frac{1}{2}I^A_{cc}+T^A_{cc} & 0 & 0 & 0 & I^{AB}_{cc} \\ T^{A*}_{cu} & -S^A_{ct} & -\frac{1}{2}I^A_{cc}+T^{A*}_{cc} & -S^A_{cc} & 0 & 0 & 0 & 0 \\ 0 & 0 & 0 & 0 & -U^B_{uu} & T^B_{ut} & -U^B_{uc} & T^B_{uc} \\ 0 & 0 & 0 & 0 & T^{B*}_{tu} & -S^B_{tt} & T^{B*}_{tc} & -S^B_{tc} \\ 0 & 0 & 0 & 0 & -U^B_{cu} & T^B_{ct} & -U^B_{cc} & \frac{1}{2}I^B_{cc}+T^B_{cc} \\ 0 & 0 & I^{BA}_{cc} & 0 & T^{B*}_{cu} & -S^B_{ct} & \frac{1}{2}I^B_{cc}+T^{B*}_{cc} & -S^B_{cc} \end{pmatrix},$$

$$\begin{pmatrix} MATRIX \\ II \end{pmatrix} = \begin{pmatrix} U^A_{ut} & -\frac{1}{2}I^A_{uu}-T^A_{uu} & 0 & 0 \\ \frac{1}{2}I^A_{tt}-T^{A*}_{tt} & S^A_{uu} & 0 & 0 \\ U^A_{ct} & -T^A_{cu} & 0 & 0 \\ -T^{A*}_{ct} & S^A_{cu} & 0 & 0 \\ 0 & 0 & U^B_{ut} & -\frac{1}{2}I^B_{uu}-T^B_{uu} \\ 0 & 0 & \frac{1}{2}I^B_{tt}-T^{B*}_{tt} & S^B_{uu} \\ 0 & 0 & U^B_{ct} & -T^B_{cu} \\ 0 & 0 & -T^{B*}_{ct} & S^B_{cu} \end{pmatrix}.$$

In the previous relations I denotes the identity operator with the subscripts and superscripts specifying the part of the boundary where it is considered.

As the functions ψ^η and φ^η respectively represent the virtual displacements or tractions and the system in (23) has to be satisfied for any virtual function, the columns containing these functions could be omitted to obtain a symmetric BIE system for DDBVP. Nevertheless, for the SGBEM formulation it is more convenient to keep (23) in the present form.

4 Discretization

The BIE system (23) will be solved numerically by SGBEM. To this end, let us introduce an approximation of the functions appearing there by continuous linear boundary elements [París and Cañas (1997)] (allowing discontinuities of the tractions at the junctions of the elements if required). Thus, the approximation formulas can be written in the form:

$$u^\eta(x) = \sum_k N^\eta_{\psi k}(x)\mathrm{u}^\eta_k, \quad t^\eta(x) = \sum_k N^\eta_{\varphi k}(x)\mathrm{t}^\eta_k, \tag{24}$$

where $N^\eta_{\psi k}(x)$ and $N^\eta_{\varphi k}(x)$, respectively, are matrices containing the shape functions of displacements and tractions associated to node k at Γ^η, and u^η_k and t^η_k, respectively, are vectors containing the components of the displacement and traction vector at node k. Let u^η, g^η, t^η and h^η, respectively, denote the vector containing all unknown nodal displacements, all prescribed nodal displacements, all unknown nodal tractions and all prescribed nodal tractions associated to Γ^η. Let the subvectors of the nodal unknowns at the boundary parts Γ^η_u, Γ^η_t and Γ_c, respectively, be distinguished by the same subscripts u, t and c. The set of vectors of virtual functions ψ^η and φ^η can be chosen in such a way that they are equal to shape functions pertinent to each nodal unknown. Such a choice leads to the square symmetric matrix of the following system of linear algebraic equations:

$$\begin{pmatrix} MATRIX \\ III \end{pmatrix} \begin{pmatrix} \mathrm{t}^A_u \\ \mathrm{u}^A_t \\ \mathrm{t}^A_c \\ \mathrm{u}^A_c \\ \mathrm{t}^B_u \\ \mathrm{u}^B_t \\ \mathrm{t}^B_c \\ \mathrm{u}^B_c \end{pmatrix} = \begin{pmatrix} MATRIX \\ IV \end{pmatrix} \begin{pmatrix} \mathrm{h}^A \\ \mathrm{g}^A \\ \mathrm{h}^B \\ \mathrm{g}^B \end{pmatrix}. \tag{25}$$

where

$$\begin{pmatrix} MATRIX \\ III \end{pmatrix} = \begin{pmatrix} -\mathrm{U}^A_{uu} & \mathrm{T}^A_{ut} & -\mathrm{U}^A_{uc} & \mathrm{T}^A_{uc} & 0 & 0 & 0 & 0 \\ \mathrm{T}^{AT}_{tu} & -\mathrm{S}^A_{tt} & \mathrm{T}^{AT}_{tc} & -\mathrm{S}^A_{tc} & 0 & 0 & 0 & 0 \\ -\mathrm{U}^A_{cu} & \mathrm{T}^A_{ct} & -\mathrm{U}^A_{cc} & -\frac{1}{2}\mathrm{M}^A_{cc}+\mathrm{T}^A_{cc} & 0 & 0 & 0 & \mathrm{M}^{AB}_{cc} \\ \mathrm{T}^{AT}_{cu} & -\mathrm{S}^A_{ct} & -\frac{1}{2}\mathrm{M}^{AT}_{cc}+\mathrm{T}^{AT}_{cc} & -\mathrm{S}^A_{cc} & 0 & 0 & 0 & 0 \\ 0 & 0 & 0 & 0 & -\mathrm{U}^B_{uu} & \mathrm{T}^B_{ut} & -\mathrm{U}^B_{uc} & \mathrm{T}^B_{uc} \\ 0 & 0 & 0 & 0 & \mathrm{T}^{BT}_{tu} & -\mathrm{S}^B_{tt} & \mathrm{T}^{BT}_{tc} & -\mathrm{S}^B_{tc} \\ 0 & 0 & 0 & 0 & -\mathrm{U}^B_{cu} & \mathrm{T}^B_{ct} & -\mathrm{U}^B_{cc} & \frac{1}{2}\mathrm{M}^B_{cc}+\mathrm{T}^B_{cc} \\ 0 & 0 & \mathrm{M}^{BA}_{cc} & 0 & \mathrm{T}^{BT}_{cu} & -\mathrm{S}^B_{ct} & \frac{1}{2}\mathrm{M}^{BT}_{cc}+\mathrm{T}^{BT}_{cc} & -\mathrm{S}^B_{cc} \end{pmatrix},$$

$$\begin{pmatrix} MATRIX \\ IV \end{pmatrix} = \begin{pmatrix} \mathrm{U}^A_{ut} & -\frac{1}{2}\mathrm{M}^A_{uu}-\mathrm{T}^A_{uu} & 0 & 0 \\ \frac{1}{2}\mathrm{M}^A_{tt}-\mathrm{T}^{AT}_{tt} & \mathrm{S}^A_{uu} & 0 & 0 \\ \mathrm{U}^A_{ct} & -\mathrm{T}^A_{cu} & 0 & 0 \\ -\mathrm{T}^{AT}_{ct} & \mathrm{S}^A_{cu} & 0 & 0 \\ 0 & 0 & \mathrm{U}^B_{ut} & -\frac{1}{2}\mathrm{M}^B_{uu}-\mathrm{T}^B_{uu} \\ 0 & 0 & \frac{1}{2}\mathrm{M}^B_{tt}-\mathrm{T}^{BT}_{tt} & \mathrm{S}^B_{uu} \\ 0 & 0 & \mathrm{U}^B_{ct} & -\mathrm{T}^B_{cu} \\ 0 & 0 & -\mathrm{T}^{BT}_{ct} & \mathrm{S}^B_{cu} \end{pmatrix}$$

The elements of the submatrices denoted with letters U, T and S are formed by double integrals

including the integral kernel denoted by the same letter as is usual in SGBEM. The square submatrices of order d, associated to nodes k and l, of the mass matrices M^{η}_{rr}, with r being u, t or c, are formed by the integrals:

$$
\begin{aligned}
(\mathrm{M}^{\eta}_{uu})_{kl} &= \int_{\Gamma^{\eta}_{u}} N^{\eta}_{\varphi k}(x) N^{\eta}_{\psi l}(x) \mathrm{d}_x S, \\
(\mathrm{M}^{\eta}_{tt})_{kl} &= \int_{\Gamma^{\eta}_{t}} N^{\eta}_{\psi k}(x) N^{\eta}_{\varphi l}(x) \mathrm{d}_x S, \\
(\mathrm{M}^{\eta}_{cc})_{kl} &= \int_{\Gamma_c} N^{\eta}_{\varphi k}(x) N^{\eta}_{\psi l}(x) \mathrm{d}_x S.
\end{aligned}
\tag{26}
$$

It has to be stressed that the mass matrices M^{AB}_{cc} and M^{BA}_{cc} do not have to be square, as there is no requirement on the identity of the meshes used to approximate displacements and tractions along both sides of Γ_c. In fact, the displacements u^A_c can be approximated using a mesh distinct from that used for the approximation of u^B_c, and an analogous statements holds for tractions t^B_c and t^A_c. Recall also that shape functions of displacements and tractions defined along one side of Γ_c can be different as well. In other words, each of the bodies can be meshed independently, obtaining two nonconforming meshes along Γ_c. In this situation, the aforementioned matrices, respectively, are associated to a discrete L_2-projection from the space of the shape functions (restricted to Γ_c) of Ω^B on the space of the shape functions (restricted to Γ_c) of Ω^A and viceversa. The elements of these matrices can be represented by the integrals:

$$
(\mathrm{M}^{AB}_{cc})_{kl} = \int_{\Gamma_c} N^{A}_{\varphi k}(x) N^{B}_{\psi l}(x) \mathrm{d}_x S. \tag{27}
$$

In order to obtain a symmetric matrix on the left-hand side of (25) the following requirement should hold:

$$
\mathrm{M}^{BA}_{cc} = (\mathrm{M}^{AB}_{cc})^T. \tag{28}
$$

Note that this always holds in the case where the geometrical approximations of Γ_c by boundary element meshes on Ω^A and Ω^B sides coincide, although nodes and shape functions of these meshes do not need to coincide. This typically happens in the case of Γ_c given by a straight line (in 2-*D*) or by a plane surface with a polygonal boundary (in 3-*D*). If Γ_c is curved, one possible way to keep this property is to calculate the integrals over the common-refinement mesh, see Jiao and Heath (2004). This approach for calculating the integral in (28) is sketched at Figure 3. The nodal shape functions $N^A_{\varphi k}$ and $N^B_{\psi l}$ have the common support over the segments denoted by a, b and c. Over these portions of the common-refinement mesh the integral is evaluated considering the actual values of the shape functions. Due to the curvature of Γ_c, a piecewise straight boundary element approximation of Γ_c exhibits jumps in the normal vector. These jumps do not coincide for the nonconforming meshes along both sides of Γ_c. Therefore, the best way to evaluate the vectorial elastic variables at Γ_c is to consider their components in the global coordinate system x_i.

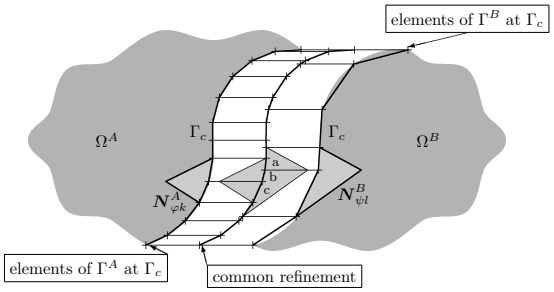

Figure 3: Common-refinement concept.

5 Numerical examples

5.1 Example definitions and discretizations

The following three examples, Figure 4, have been chosen to study the accuracy and convergence of the proposed approach. A fictitious partition of a homogeneous domain Ω has been performed, originating two subdomains Ω^A and Ω^B with the same material parameters, in all these examples. The Lame constants have been chosen $\lambda = \mu$. The three examples have known analytical solutions, variations of displacements and tractions (expressed in cartesian coordinates) along the interface Γ_c being nonlinear in all the cases. To test the behaviour of the approach developed for different shapes of Γ_c, an open straight, an open curved, and a closed curved interface Γ_c

have been considered, respectively, in the first, second and third examples.

Rectangular plate under exponential load. Consider a rectangular domain Ω partitioned into two square subdomains Ω^A and Ω^B, Figure 4(a). The solution is given by the Airy stress function: $F(x_1,x_2) = \sin(x_1)\exp(-x_2)$, the type of boundary conditions being defined as shown in Figure 4(a). The uniform boundary element meshes are defined as follows: starting from 2 elements per edge of a subdomain in the coarsest mesh and refining them by dividing each element into 2. Seven progressively refined meshes are used (with 2, 4, 8, 16, 32, 64 and 128 elements along each edge). For the nonconforming meshes along Γ_c, the 'two-elements per five-elements' relation is used, which means 2–5, 4–10, 8–20, 16–40, 32–80, 64–160 and 128–320 elements at both sides of Γ_c. The results are plotted for the points of Γ_c — the segment AB, coordinate s being the distance of the current point from point A.

Ring under circumferential shear. Consider a ring, subjected to a constant shear stress along the exterior face and fixed along its inner face. Due to the antisymmetric character of this problem, the domain Ω is given by a quarter of the ring. It is partitioned into Ω^A and Ω^B as shown in Figure 4(b). The meshes, which are uniform at each edge of a subdomain, are defined as follows: starting from 2 elements per straight edge and 3 elements per circular edge in the coarsest mesh and refining them by dividing each element into 2. Six progressively refined meshes are used (with 2(3), 4(6), 8(12), 16(24), 32(48) and 64(96) elements at a straight (circular) edge). For the nonconforming meshes along Γ_c, the 'three-elements per seven-elements' relation is applied, which means 3–7, 6–14, 12–28, 24–56, 48–112 and 96–224 elements at both sides of Γ_c. The results are plotted for the points of Γ_c, the arc AB, coordinate α being the angle between the radius vector of the current point and the radius vector OA.

Square plate under uniaxial compression. Consider a square domain Ω, which is subjected to compression, partitioned into a circular subdomain Ω^A and its complementary subdomain Ω^B, Figure 4(c). The meshes, which are uni-

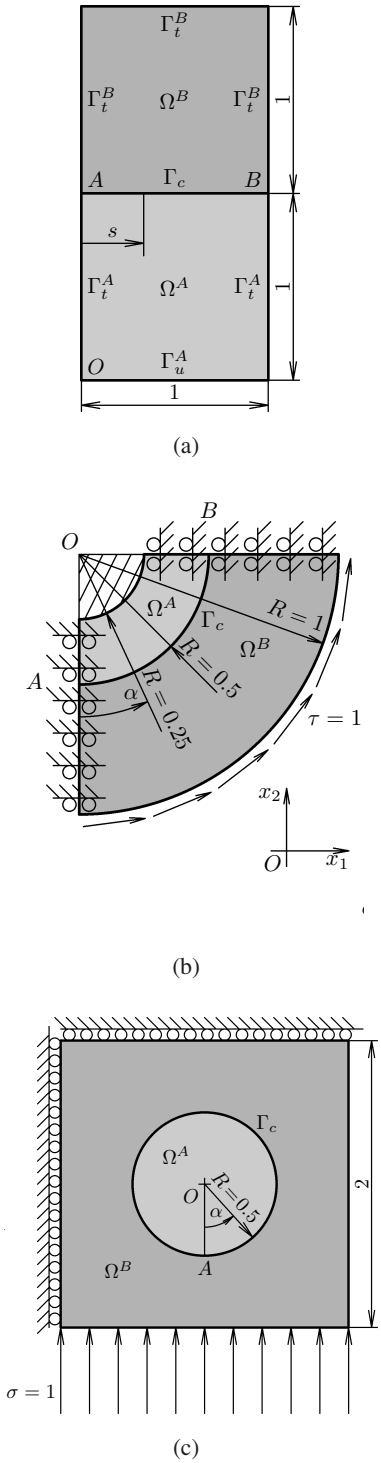

Figure 4: Examples. (a) Rectangular plate under exponential load, (b) Ring under circumferential shear, (c) Square plate under uniaxial compression.

form at each edge, are defined as follows: starting from 8 elements per straight edge and 12 elements at the circumference and refining them by dividing each element into 2. Four progressively refined meshes are used (with 8(12), 16(24), 32(48) and 64(96) elements at an edge (the circumference)). For the nonconforming meshes along Γ_c, the 'three-elements per seven-elements' relation is applied, which means 12–28, 24–56, 48–112 and 96–224 elements at both sides of Γ_c. The results are plotted for the points of Γ_c — the circumference, coordinate α being the angle between the radius vector of the current point and the radius vector OA, measured counterclockwise.

5.2 Error evaluation

The present analysis is concerned with the behaviour of the numerical solutions obtained along Γ_c. Let the numerical solution of a problem (displacement or traction vector defined along Γ_c) be denoted generically as z_n and the analytical one as z_a.

The absolute error, which is simply the difference $z_n(x) - z_a(x)$ given at a point $x \in \Gamma_c$, is presented first. In the presented plots this error is approximated linearly between the nodes.

The following two discretized error norms have been chosen to characterize the covergence behaviour of the method along Γ_c, presenting the convergence of the error in the integral L_2-norm and in the maximum-norm. The former is expected to present a regular convergence behaviour, whereas the latter is of major interest for engineers, who are typically interested in maximum values of displacements or stresses, respectively, applied in the so-called 'stiffness' and 'strength' criteria.

Integral L_2-norm of error defined as:

$$\|z_n - z_a\|_{L_2} = \sqrt{\int_{\Gamma_c} \sum_{l=1}^{2} \big(z_{nl}(x) - z_{al}(x)\big)^2 \mathrm{d}_x S} \quad (29)$$

is approximated using the Gaussian quadrature along the discretized Γ_c as follows (for the sake of simplicity Γ_c is considered to be straight in the formula):

$$\|z_n - z_a\|_{L_2} \approx \sqrt{\sum_{i=1}^{N_c} \sum_{k=1}^{N_g} \sum_{l=1}^{2} \big(z_{nl}(x_i^k) - z_{al}(x_i^k)\big)^2 w_i^k}, \quad (30)$$

where N_c is the number of elements used in evaluation of z_n at Γ_c, N_g is the number of Gauss points per element ($N_g = 16$ has been chosen), x_i^k is the k-th Gauss point of the i-th element and w_i^k is the weight of the k-th Gauss point multiplied by half of the length of the i-th element. Then, $z_a(x_i^k)$ is the value of the analytical solution at x_i^k, while $z_n(x_i^k)$ is the value of the linear approximation of the numerical solution between two nodes of the i-th element.

Maximum-norm of error is defined as the maximum of absolute error achieved over all nodes for a particular mesh:

$$\|z_n - z_a\|_{\mathrm{MAX}} = \max_{x_i - \mathrm{node}} \max_{l=1,2} \big|z_{nl}(x_i) - z_{al}(x_i)\big|. \quad (31)$$

Convergence rate for an h refinement is defined as the number β for which there exists a constant c such that relation

$$\|z_n^N - z_a\| \approx c \cdot N^{-\beta} \|z_a\|, \quad (32)$$

holds for a selected error norm, N giving the characteristic number of elements of a mesh and z_n^N giving the numerical solution for this particular mesh.

5.3 Solution and error distribution.

The present analysis of numerical results starts with the study of the magnitude, distribution and smoothness of the solution error. For each particular example one of the aforementioned meshes along the exterior boundary Γ is selected, three discretizations of Γ_c being considered: $N^A < N^B$, $N^A > N^B$ and $N^A = N^B$, where N^A and N^B are the numbers of elements along Γ_c on Γ^A and Γ^B side respectively. For example the choice 4–10 corresponds to $N^A = 4$, $N^B = 10$ if $N^A < N^B$, $N^A = 10$, $N^B = 4$ if $N^A > N^B$ and $N^A = N^B = 4$ if $N^A = N^B$. Each line in the presented plots corresponds to a

discretization of Γ_c and either to the coarser or to the finer mesh, a letter in parentheses indicating the corresponding subdomain.

In order to deal with comparable values and errors of displacements and tractions, displacement values are scaled by factor μ, values $u^* = \mu u$ and the corresponding errors then being presented. Due to the fact that the tractions t_c^A and t_c^B have opposite signs, the latter is plotted with the changed sign.

5.3.1 Rectangular plate under exponential load

Numerical results are presented for meshes 16–40 along Γ_c. The displacement errors are plotted at Figure 5. It is easy to observe that results for one mesh behave differently from the rest of the meshes, namely the displacements at the finer mesh in the case $N^A > N^B$, i.e. at Γ^A side of Γ_c, oscillate more strongly than the other displacement solutions. Nevertheless, as can be observed, these oscillations are rather regular. If the node of Γ^A coincides with the node of Γ^B, the errors practically coincide, and also at the nodes of Γ^A close to some nodes of Γ^B the error is similar to the error at the corresponding nodes of Γ^B. This relation between errors is repeated as a pattern corresponding to the repeated pattern 2–5 of this non-conforming discretization of Γ_c.

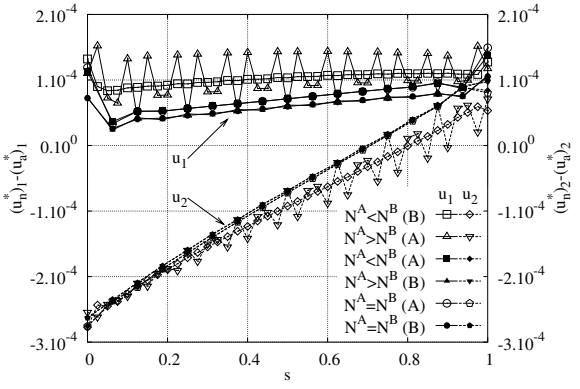

Figure 5: Rectangular plate under exponential load. Displacement errors, meshes 16–40.

This behaviour is explained in a simple way at Figure 6. The meshes along both sides of Γ_c represent the above mentioned pattern 2–5. Square and circle marks, respectively, correspond to the coarser and finer meshes. If the solution at the coarser mesh were exact, the square marks would lie exactly on the curve giving the exact solution, as indicated. If the nodes of the finer and coarser meshes coincide, as in our case, at the end-points of the pattern interval, then the coarse-mesh and the fine-mesh solution may also coincide at those points. However, the displacement solutions along Γ_c, have to satisfy the compatibility condition represented by the first integral in (10e), which means the fulfillment of this condition at Γ^A. Considering $N^A > N^B$ there are only a few 'prescribed boundary data' represented by u_c^B in (10e), but many linear conditions generated by δt_c^A. This causes the linearization of the solution at Γ^A, i.e. at the finer mesh. Therefore, instead of seeking a solution close to the analytical solution, the numerical procedure looks for the values, marked by filled circles, lying approximately on the coarser-mesh solution. This can cause larger errors than expected at some nodes of the finer mesh and consequently produce oscillations in the error distribution, as observed in Figure 5.

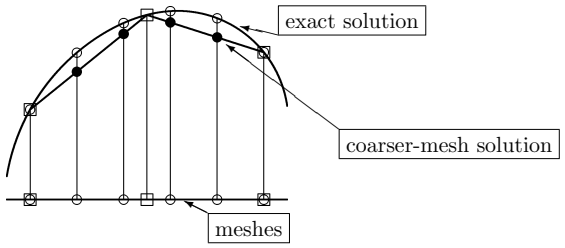

Figure 6: Relation of the mesh pattern and error patterns.

These strong oscillations of error, however, are not present in the case $N^A < N^B$, Figure 5. This could lead to a conclusion that the displacements u_c^B represent primary unknowns used for the calculation of u^A as secondary unknowns. Actually, a theoretical analysis, similar to that introduced in Núñez *et al.* (2003) for a classical BEM, developed in Appendix for a simple kind of DDBVP solved by SGBEM, confirms this conclusion, see (A23). Thus, when u_c^B is defined at the finer mesh a significant reduction in the error at this mesh could be observed, as indicated

by unfilled circles in Figure 6 lying on the analytic solution, whereas the values of u_c^A defined on the coarser mesh, the filled squares if they were marked, could also lie close to the analytic solution, almost at the same positions as unfilled squares.

Nevertheless, it has to be stressed that the magnitude of the nodal errors is relatively small in all cases, no influence of them being seen on the plot of displacements in Figure 7, where only displacements obtained at the finer meshes of the nonconforming discretizations are presented.

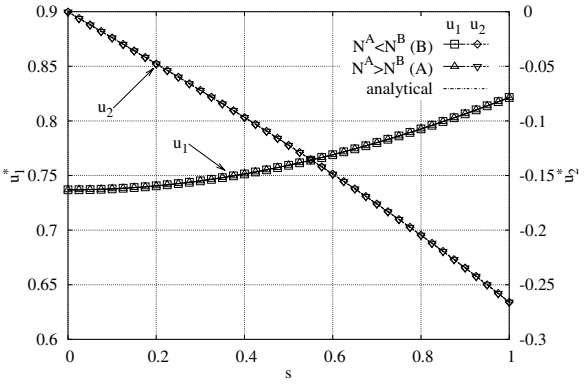

Figure 7: Rectangular plate under exponential load. Displacement distributions, meshes 16–40.

It is also interesting to compare results obtained by the conforming and nonconforming discretizations, Figure 5. The displacements at the conforming mesh approximately coincide with the displacements at the coarser meshes, i.e. displacements along Γ^A or Γ^B, respectively, coincide with the displacements at the mesh along Γ^A in the case $N^A < N^B$ (check the unfilled circle and the filled square marks for the component u_1) or at the mesh along Γ^B in the case $N^A > N^B$ (the filled circle marks and the filled triangle marks for the same component). However, there exists a small gap between the results from both faces of the interface in the case of the conforming discretization.

When analyzing traction solutions it is instructive to start comparing tractions obtained by the nonconforming discretizations. Looking at traction values obtained at the finer meshes in Figure 8, oscillations can be observed for the case $N^A > N^B$ whereas no oscillations are visible for the case $N^A < N^B$. The enormous difference between these two cases can be seen in the plots of the error distribution in Figure 9 (bottom). Nevertheless, repeating patterns of errors, similar to those observed in displacement solutions but multiplied in magnitude, can be observed in these traction solutions as well. This could lead to a conclusion that displacements are the primary unknowns and the tractions are calculated from them as secondary unknowns. Actually, the theoretical analysis in Appendix, confirms this conclusion, see (A22) and (A27). Thus, if displacements exhibit oscillations of errors, the corresponding tractions exhibit them as well and their magnitude is increased, caused by the integral operator applied.

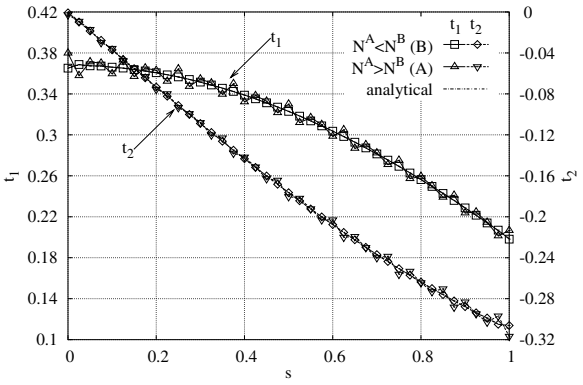

Figure 8: Rectangular plate under exponential load. Traction distributions, finer meshes, meshes 16–40.

Studying distribution of traction errors at other meshes shown in Figure 9 (top) it is seen that their magnitudes are comparable with the finer mesh errors in the case $N^A < N^B$. Nevertheless, the largest oscillations can again be observed in the coarser mesh solution in the case $N^A > N^B$. There is also another important fact which should be noted: the strongest oscillations appear near the end-points of Γ_c (corners of the adjacent subdomains) for all the cases, including the conforming mesh solution. This fact might cause different values of rate of convergence in the applied norms of error, Section 5.4.1.

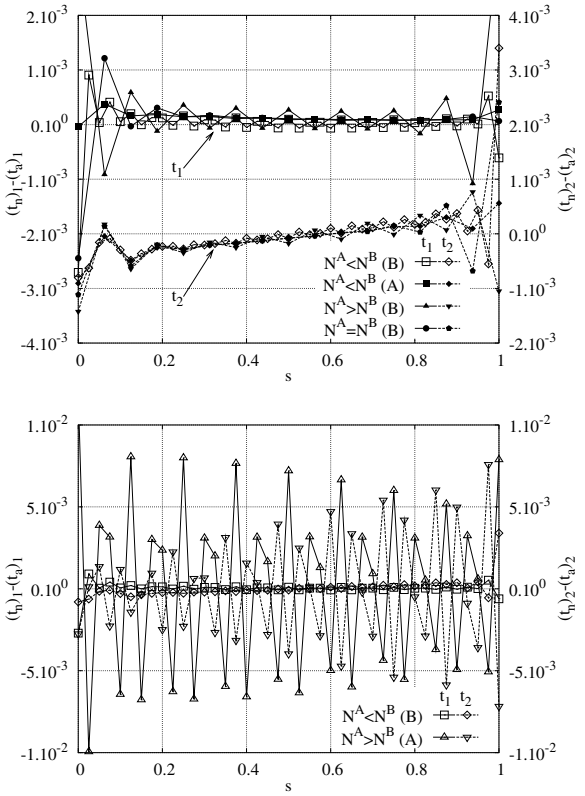

Figure 9: Rectangular plate under exponential load. Traction errors, meshes 16–40, all meshes (top), finer meshes (bottom).

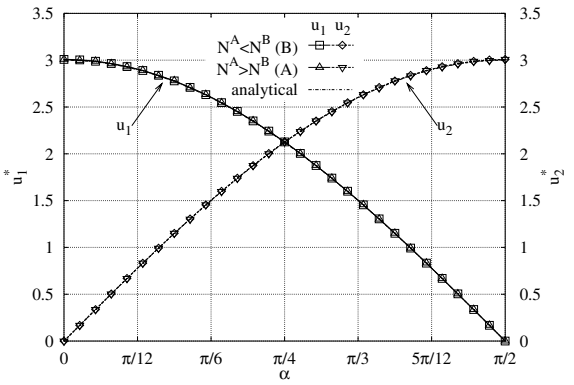

Figure 10: Ring under circumferential shear. Displacement distributions, finer meshes, meshes 12–28.

As already mentioned, the reasons for the above observed strong oscillatory behaviour of tractions at the finer mesh when $N^A > N^B$ are discussed, studying a simple DDBVP in more detail and analyzing the numerical procedure of the solution of the linear equation system, in Appendix and especially in part Appendix A.3 where an explanation of these oscillations is given.

5.3.2 *Ring under circumferential shear*

Numerical results are presented for meshes 12–28 along Γ_c. The displacements obtained at the finer meshes of the nonconforming discretizations shown in Figure 10 approximate very well the analytic solution. Due to the fact that the displacement components u_1 and u_2 are mutually symmetric with respect to the angle $\alpha = \frac{\pi}{4}$ ($u_1(\alpha) = u_2(\frac{\pi}{2} - \alpha)$), only results for u_1 will be presented in what follows.

In Figure 11, where displacement errors are plotted, a strong oscillatory behaviour of the error obtained at the finer mesh in the case $N^A > N^B$ is again observed, in contrast with a relatively smooth distribution of the error at other meshes. Nevertheless, in much the same way as was already observed in the previous example, these oscillations are rather regular. The pattern of the nonconforming discretization is 3–7 in the present case, each third node of the coarser mesh coinciding with each seventh node of the finer mesh. The same pattern is repeated in the displacement errors as can be seen in Figure 11 looking at the triangle marks, filled and unfilled. The explanation given in the previous example, see Figure 6, can be applied here as well.

Let the consistency error, which represents the accuracy of the approximation of the interface conditions by nonconforming discretizations, be defined as the difference of the solutions, or equivalently of their absolute errors, at the adjacent sides of Γ_c. It is interesting to observe in Figure 11 that the consistency error of displacements of a similar magnitude as in the case $N^A > N^B$ appears also in the case $N^A < N^B$. Nevertheless, in the latter case this consistency error is rather smooth in comparison with the former case.

Notice that the maximum value of the absolute error is achieved at the coarser mesh in the case $N^A < N^B$ and that the conforming discretization

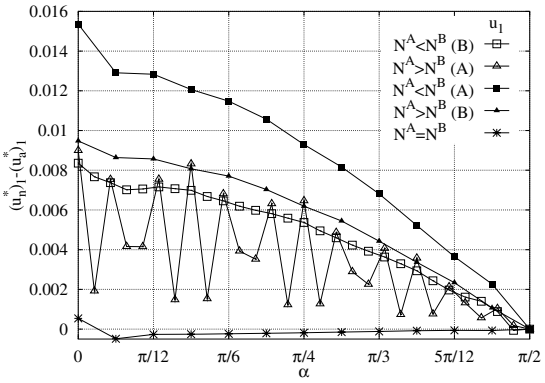

Figure 11: Ring under circumferential shear. Displacement errors, meshes 12–28.

provides substantially smaller errors than the non-conforming discretizations.

When comparing displacement and traction solutions obtained at the finer meshes of the non-conforming discretizations, Figures 10 and 12, it is seen that the oscillatory behaviour of displacements in the case $N^A > N^B$ is substantially magnified in the case of tractions, whereas traction oscillations in the case $N^A < N^B$ are hardly visible. The substantial difference between the magnitude of errors in these two cases is clearly seen in Figure 13 (bottom), where, due to the above mentioned symmetry, only the component t_1 is plotted.

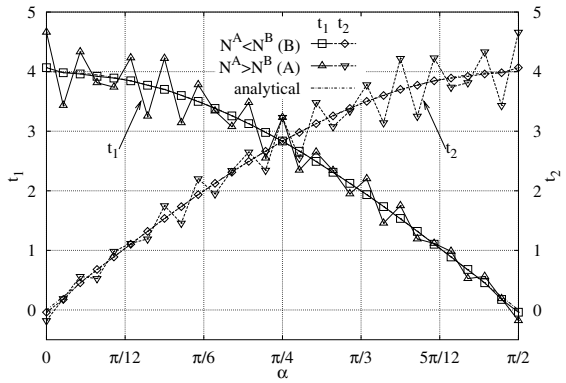

Figure 12: Ring under circumferential shear. Traction distributions, finer meshes, meshes 12–28.

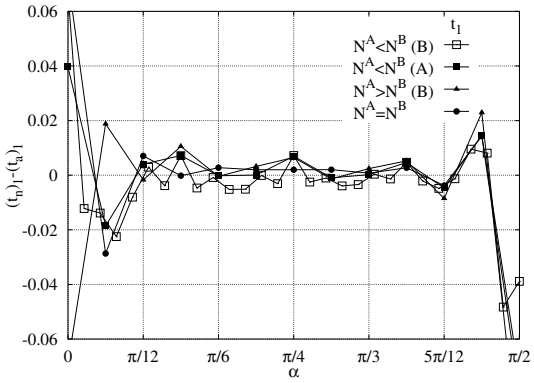

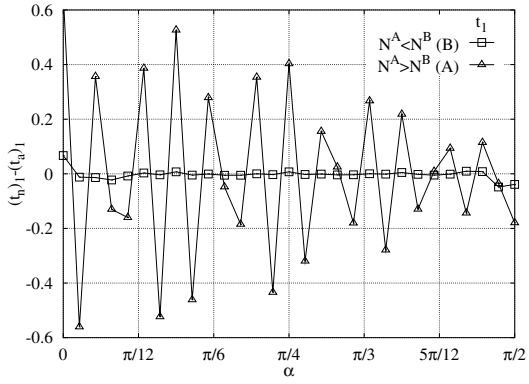

Figure 13: Ring under circumferential shear. Traction errors, meshes 12–28, all meshes (top), finer meshes (bottom).

Traction error distributions at all meshes, except for the finer mesh in the case $N^A > N^B$ (which has been omitted due to being out of the applied scale), shown in Figure 13 (top), have similar magnitude. All these errors seem to have some oscillations, the smallest errors being achieved in the case of the conforming mesh, though close to the end-points of Γ_c (corners of the adjacent subdomains) there are significant oscillations also in this case.

The character of the strong oscillations of traction errors in the case $N^A > N^B$ is illustrated considering the finest mesh 96–224, with the pattern 3–7 shown in Figure 14 (top) for the coarsest case. It should be noted, and it is also visible in the picture, that there are gaps and overlappings along the interface separating the discretized subdomains. The inner nodes of the pattern are marked by triangles, the end-points be-

ing marked by circles. Surprisingly smooth lines in Figure 14 (bottom) represent traction errors obtained at the subsets of the pattern nodes (denoted by numbers 1 to 6 or letters *a* or *b* according to the top drawing) repeated along Γ_c, the substantially smaller errors at the coarser mesh being multiplied by an ad-hoc factor of value 100. For example, the two lines of circles representing the end points of the pattern for both the finer and coarser meshes coincide, the character of the error at those points being the same but the magnitude being substantially different.

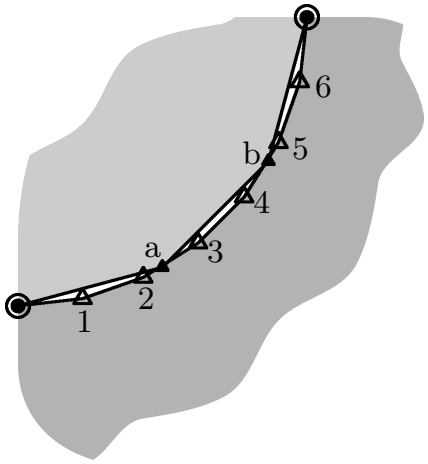

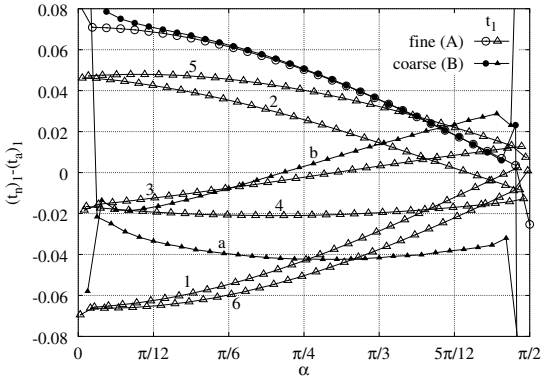

Figure 14: Ring under circumferential shear. Mesh pattern '3–7' (top), traction errors in the case $N^A > N^B$, mesh 96–224 (bottom).

5.3.3 Square plate under uniaxial compression

This example differs from the previous ones in that the curved interface is closed, a possible influence of the interface end-points on the error behaviour thus being eliminated.

The displacements along Γ_c obtained at the finer meshes of the nonconforming discretizations are shown in Figure 15, an excellent approximation of the analytical solution again being obtained. Notice that expressions of u_1 and u_2 along Γ_c in terms of α include, due to the curvature of Γ_c, trigonometric functions.

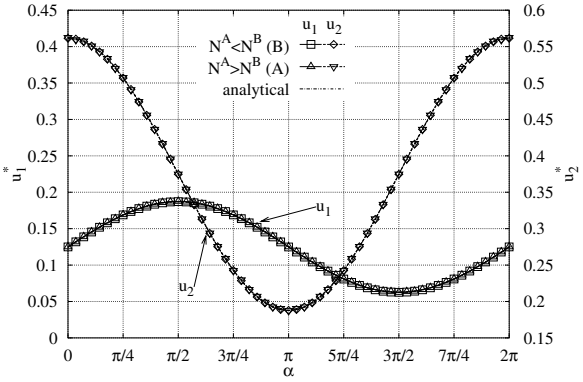

Figure 15: Square plate under uniaxial compression. Displacement distributions, finer meshes, meshes 24–56.

Figure 16 shows the displacement error distributions, a strong oscillatory behaviour of the finer mesh in the case $N^A > N^B$ following the discretization pattern, 3–7 in the present case, being observed as in the previous examples.

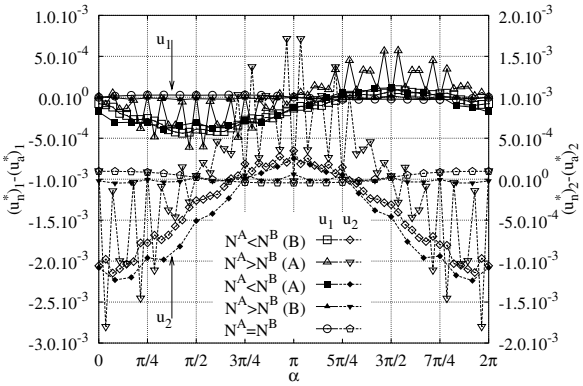

Figure 16: Square plate under uniaxial compression. Displacement errors, meshes 24–56.

The behaviour of the displacement errors in Figure 16 for the rest of the meshes is rather smooth. A small consistency error appears in the case $N^A < N^B$, the compatibility condition being only slightly violated. Although the error achieved by the conforming-mesh is apparently the smoothest one, the error at the coarser mesh in the case $N^A > N^B$ is surprisingly somewhat smaller.

Tractions obtained at finer meshes of the nonconforming discretizations, Figure 17, show similar behaviour to the previous examples, oscillations being visible in the case $N^A > N^B$ in t_2 and also in t_1 (whose analytic value is zero), though smaller ones, as could be expected.

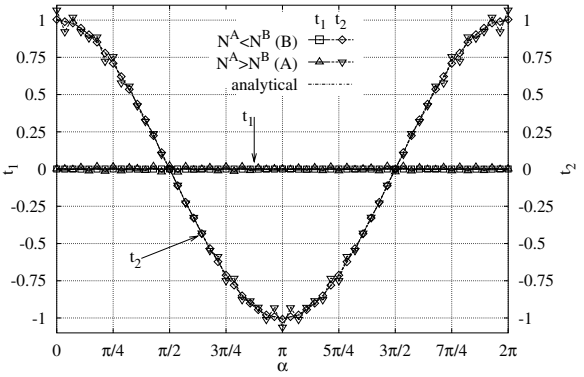

Figure 17: Square plate under uniaxial compression. Traction distributions, finer meshes, meshes 24–56.

Figure 18 (bottom) shows traction errors at finer meshes of the nonconforming discretizations, typically strong oscillations being observed in the case $N^A > N^B$. Oscillations of traction errors in the case $N^A < N^B$, almost invisible in Figure 18 (bottom), can be seen in Figure 18 (top), where the results for the finer mesh of the case $N^A > N^B$ have been omitted, being out of the present scale. The repeating pattern of the errors is now also observable for the case $N^A < N^B$. The absence of endpoints on a smooth Γ_c yields a very smooth traction error distribution in the conforming case.

Finally, it should be mentioned that, whereas in the previous two examples the choice of the subdomains Ω^A and Ω^B was arbitrary, with no relevance to the numerical results, in the present

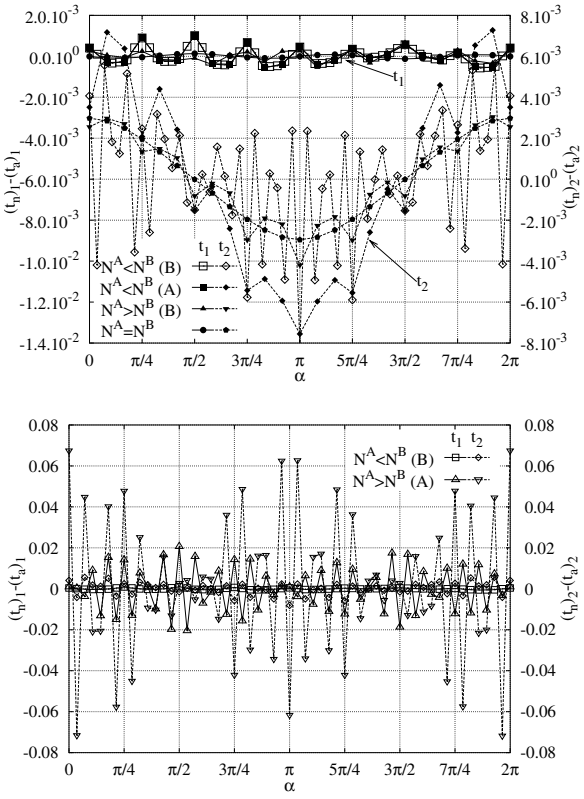

Figure 18: Square plate under uniaxial compression. Traction errors, meshes 24–56, all meshes (top), finer meshes (bottom).

example subdomain Ω^A should be the circle as shown in Figure 4(c). This is related to the problem of the invertibility of the SGBEM system for a single domain BVP with cavities subjected to traction (Neumann) boundary conditions, studied in Vodička *et al.* (2006). To avoid the above restriction on the choice of the interior subdomain, some of the techniques developed in Vodička *et al.* (2006) could be used.

5.4 Error convergence

Convergence of displacement and traction errors along Γ_c in the discretized L_2- and *MAX*-norms for *h*-refinements of boundary element meshes is studied for all the above examples. Dependence of an error norm on the number N, defined as the minimum number of elements along Γ_c belonging to one of the bodies, i.e. $N = \min(N^A, N^B)$, is plotted in log-log scale. For each refinement,

given by N, results for the following three discretizations are presented: $N = N^A < N^B$, $N^A > N^B = N$ and $N = N^A = N^B$. Each line in the plot corresponds to a discretization of Γ_c and either to the coarser or to the finer mesh, a letter in parenthesis indicating the corresponding subdomain. The convergence rates β obtained by a linear regression using the three finest meshes are given in the key of the plots for each particular line.

5.4.1 Rectangular plate under exponential load

The displacement error norms computed are presented in Figure 19, the magnitude of both error norms in all cases being quite similar. All convergence rates $\beta \simeq 2$, the expected quadratic convergence of displacements for linear boundary elements thus being verified in both norms.

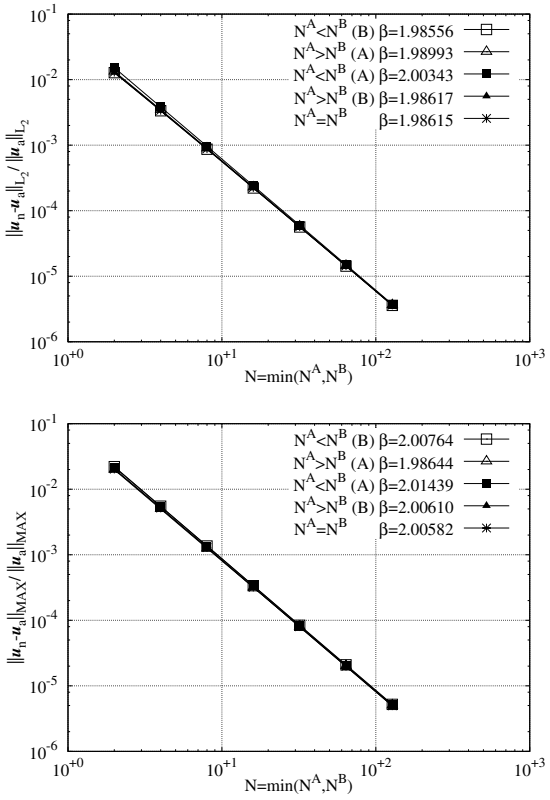

Figure 19: Rectangular plate under exponential load. Convergence rates for displacements in the L_2-norm (top) and MAX-norm (bottom).

Figure 20 presents the traction error norms obtained. Without looking at β values, it is clearly seen that the worst convergence behaviour corresponds to the finer mesh solution for $N^A > N^B$ and the best one corresponds to the coarser mesh solution for $N^A < N^B$, the other three cases having similar convergence behaviour to each other. When comparing rates of convergence in the L_2-norm, the worst case has only the linear convergence ($\beta \simeq 1$), whereas the best case is not far from the quadratic convergence ($\beta \simeq 1.85$), in the rest of the cases $\beta \simeq 1.5$. Convergence in the MAX-norm is in all cases linear, excepting the coarser mesh solution for $N^A < N^B$ where $\beta \simeq 1.37$. It should be noticed that in the latter case the convergence becomes progressively worse with increasing refinement. The above differences in the convergence behaviour are related to very large oscillations of the error at the finer mesh in the case $N^A > N^B$ and also to an increase in oscillations close to the end-points of Γ_c (corners of the adjacent subdomains), which happen in all cases, see Figure 9. This increase in oscillations naturally has stronger influence in the MAX-norm of error than in the L_2-norm. In particular, the conforming mesh solution has relatively large errors close to these corners, causing the rate of convergence in the MAX-norm to be the lowest one.

5.4.2 Ring under circumferential shear

Figure 21 shows the convergence of the displacement error norms. Convergence rates $\beta \simeq 2$ for all cases, the expected quadratic convergence of displacements again being verified in both norms. The differences between the L_2-norms of the error obtained in different cases are still relatively small, although somewhat greater than in the previous example. These differences are also small in the MAX-norm except for the conforming mesh solution, whose MAX-norm of the error is substantially smaller than in the nonconforming discretizations.

The convergence of the traction error norms is plotted in Figure 22, the worst results again being obtained by the finer mesh for $N^A > N^B$. Only linear convergence is obtained at this mesh in the L_2-norm, whereas for the rest of the meshes $\beta \simeq 1.5$. These lower rates of convergence in comparison

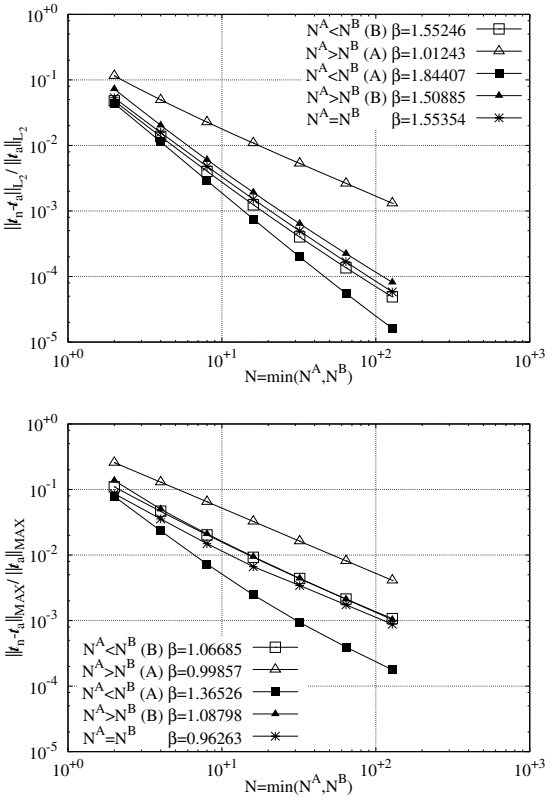

Figure 20: Rectangular plate under exponential load. Convergence rates for tractions in the L_2-norm (top) and MAX-norm (bottom).

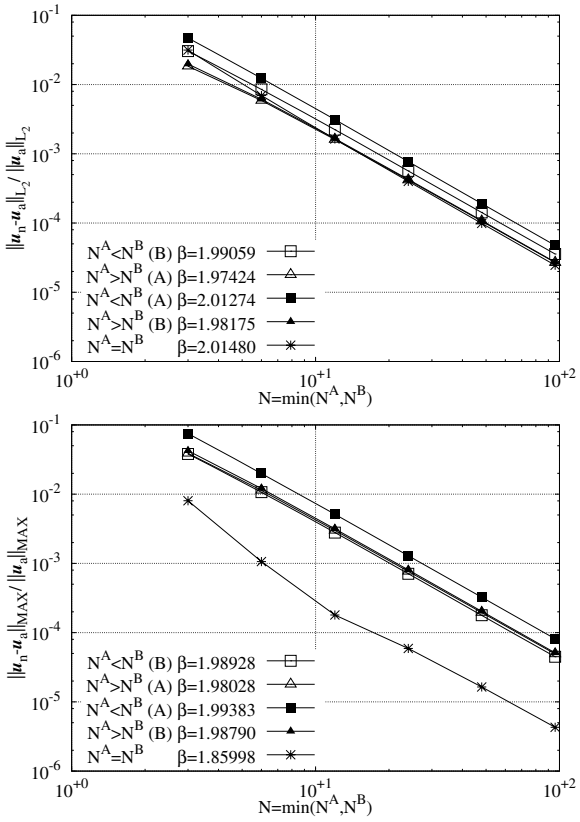

Figure 21: Ring under circumferential shear. Convergence rates for displacements in the L_2-norm (top) and MAX-norm (bottom).

with displacements might be, at least partially, related to an increase of oscillation in tractions at all meshes close to the end-points of Γ_c (corners of the adjacent subdomains). Actually, the linear rate of convergence is obtained in the MAX-norm of the error at all meshes, the greatest error norm again being obtained at the finer mesh for $N^A > N^B$.

5.4.3 Square plate under uniaxial compression

This example allows us to study whether the absence of end-points at Γ_c (corners of the adjacent subdomains) has an influence on the solution convergence. Convergence of the displacement error norms is plotted in Figure 23. The quadratic convergence of displacements in the L_2-norm is again verified, as all $\beta \simeq 2$. Notice that the smallest β is achieved by the conforming mesh. Nevertheless, evaluating β in the MAX-norm, the conforming mesh is the best one, with a very high rate of convergence $\beta \simeq 3$, the rest of the meshes giving $\beta \simeq 2$. It is also interesting that the magnitude of this error norm for the coarser mesh in the case $N^A > N^B$ is comparable with the conforming case, though its convergence rate is the smallest.

The convergence of the traction error norms is plotted in Figure 24. The worst and best convergences, approximately linear and quadratic, in both error norms have been obtained respectively by the finer mesh solution in the case $N^A > N^B$ and the conforming mesh. As can be observed in Figure 18, the error for the coarser mesh in the case $N^A > N^B$ slightly oscillates around the conforming mesh error, and consequently it could be expected that the error norms will have similar values at the both meshes. Actually, this is observed in the L_2-norm, where $\beta \simeq 1.9$ for the coarser mesh in the case $N^A > N^B$; whereas in the

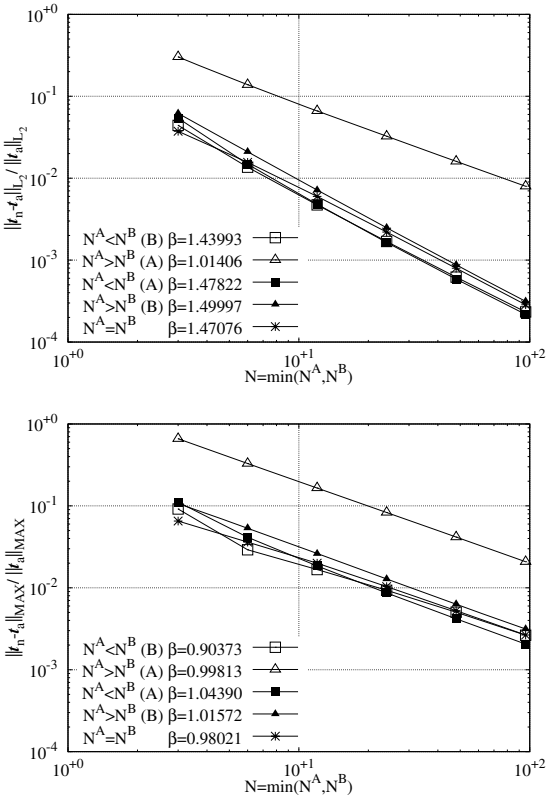

Figure 22: Ring under circumferential shear. Convergence rates for tractions in the L_2-norm (top) and MAX-norm (bottom).

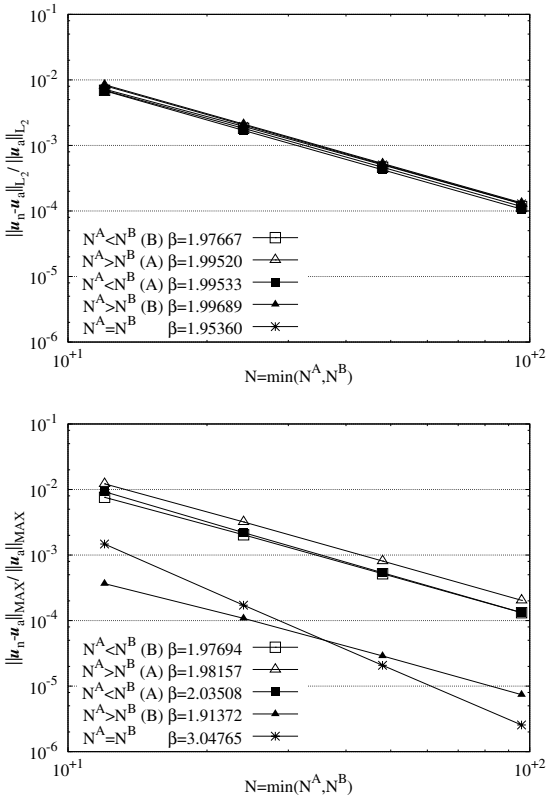

Figure 23: Square plate under uniaxial compression. Convergence rates for displacements in the L_2-norm (top) and MAX-norm (bottom).

MAX-norm a decrease in the rate of convergence is observed in this case, $\beta \simeq 1.5$, due to the above mentioned oscillations. Both meshes in the case $N^A < N^B$ present similar convergence behaviour, only slightly worse than in the conforming case, $\beta \simeq 1.6$ and $\beta \simeq 1.8$ in the L_2-norm and MAX-norm respectively.

6 Conclusions

The Symmetric Galerkin BEM approach applied to a Domain Decomposition BVP has been enriched by a possibility to formulate it through a variational principle, based on a search for a critical point of an energy functional which results in a weak formulation of the coupling conditions between the subdomains. An advantage of the method developed is that no additional unknowns, different from the natural variables of the BEM (displacements and tractions defined on the subdomain boundaries), are defined at interfaces. This method has been tested numerically using continuous linear boundary elements, very good results having been obtained for both matching and non-matching meshes at straight and curved interfaces. To the authors' knowledge, this study is the first to present a convergence study of numerical results obtained by SGBEM applied to elastic DDBVPs with non-matching meshes along curved interfaces.

The convergence of the method for h-refinements has been thoroughly studied by three examples using the discretized L_2 and maximum norms of the error. The quadratic rate of convergence, $\beta \simeq 2$, of displacements has been obtained in both norms in all the cases, as could be expected for linear elements. Nevertheless, the convergence rates for tractions have in general been found a bit lower (somewhere between linear and

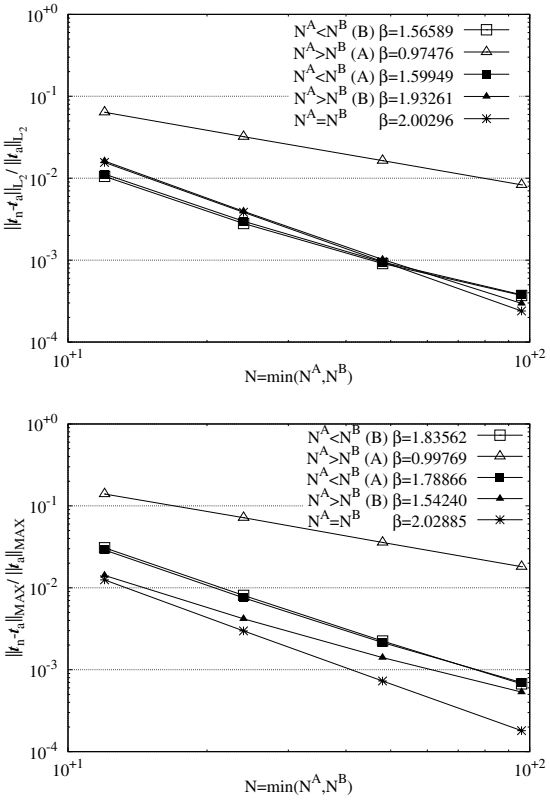

Figure 24: Square plate under uniaxial compression. Convergence rates for tractions in the L_2-norm (top) and *MAX*-norm (bottom).

quadratic, $1 \lesssim \beta \lesssim 2$), and dependent, in the case of non-matching meshes along the interface, on the choice of the subdomains, Ω^A and Ω^B, which control the tractions and displacements along the interface respectively. Reliable results in tractions on both sides of the interface, with $\beta \simeq 1.5$ in the L_2-norm, have been obtained when the more refined mesh is situated at the interface side controlling the displacements, *i.e.* $N^A < N^B$. An explanation for this observation, using a reduction of the resulting linear system to the Schur complement system, has been introduced in Appendix A.

In presence of the end-points at the interface (corners of the adjacent subdomains) the somewhat worse convergence of traction error norms observed, including the case of conforming meshes, can be, at least partially, attributed to stronger oscillations of computed tractions in the vicinity of these corners. Note that this phenomenon is usually present in BEM solutions, and thus is not specific for the present coupling approach. The solution of a problem with a smooth closed interface (without corners of the adjacent subdomains) has confirmed this explanation, as an improvement of the convergence has been observed, this improvement being substantial considering the maximum-norm of traction errors.

Acknowledgement: The work has been performed during the stay of R.V. at the University of Seville, which has been supported by a NATO Scientific Committee Fellowship (Grant number OTAF03-054). The other financial support has been given to V.M. and F.P. from the Spanish Ministry of Science and Technology (Project MAT2003-03315) and to R.V. from the Scientific Grant Agency of the Slovak Republic (Grant number 1/1089/04).

References

Aimi, A.; Diligenti, M.; Lunardini, F.; Salvadori, A. (2003): A new application of the panel clustering method for 3D SGBEM. *CMES: Computer Modeling in Engineering and Sciences*, vol. 4, pp. 31–50.

Baláš, J.; Sládek, J.; Sládek, V. (1989): *Stress Analysis by Boundary Element Method*. Elsevier, Amsterdam.

Blázquez, A.; París, F.; Mantič, V. (1998): BEM solution of two dimensional contact problems by weak application of contact conditions with non-conforming discretizations. *Int. J. of Solids and Structures*, vol. 35, pp. 3259–3278.

Blázquez, A.; Vodička, R.; París, F.; Mantič, V. (2002): Comparing the conventional displacement BIE and the BIE formulations of the first and the second kind in frictionless contact problems. *Eng. Anal. Bound. Elem.*, vol. 26, pp. 815–826.

Bonnet, M. (1995): Regularized direct and indirect symmetric variational BIE formulations for three-dimensional elasticity. *Eng. Anal. Bound. Elem.*, vol. 15, pp. 93–102.

Bonnet, M.; Maier, G.; Polizzotto, C. (1998): Symmetric Galerkin boundary element method. *Appl. Mech. Rev.*, vol. 15, pp. 669–704.

Duddeck, F.M.E. (2006): An alternative approach to boundary element methods via the Fourier transform. *CMES: Computer Modeling in Engineering and Sciences*, vol. 16, pp. 1–14.

Ganguly, S.; Layton, J.; Balakrishna, C. (2004): A coupling of multi-zone curved Galerkin BEM with finite elements for independently modelled sub-domains with non-matching nodes in elasticity. *Int. J. Num. Meth. Engrg.*, vol. 59, pp. 1021 – 1038.

Ganguly, S.; Layton, J.; Balakrishna, C.; Kane, J. (1999): A fully symmetric multizone Galerkin boundary element method. *Int. J. Num. Meth. Engrg.*, vol. 44, pp. 991 – 1009.

González, J.A.; Abascal, R. (2000): Solving rolling contact problems using boundary element method and mathematical programming algorithms. *CMES: Computer Modeling in Engineering and Sciences*, vol. 1, pp. 141–150.

Gray, L.; Paulino, G. (1997): Symmetric Galerkin boundary integral formulation for interface and multi-zone problems. *Int. J. Num. Meth. Engrg.*, vol. 40, pp. 3085 – 3101.

Guiggiani, M. (1995): Hypersingular boundary integral equations have an additional free term. *Comput. Mech.*, vol. 16, pp. 253 – 260.

Guiggiani, M.; Krishnasamy, G.; Rudolphi, T.; Rizzo, F. (1992): A general algorithm for the numerical solution of hypersingular boundary integral equations. *J. Appl. Mech.*, vol. 59, pp. 604 – 614.

Han, Z. D.; Atluri, S. N. (2002): SGBEM (for cracked local subdomain) – FEM (for uncracked global structure) alternating method for analyzing 3D surface cracks and their fatigue-growth. *CMES: Computer Modeling in Engineering and Sciences*, vol. 3, pp. 699–716.

Hartmann, F. (1985): *The Mathematical Foundation of Structural Mechanics*. Springer–Verlag, Berlin.

Hsiao, G.; Steinbach, O.; Wendland, W. (2000a): Domain decomposition methods via boundary integral equations. *J. Comp. Appl. Math.*, vol. 125, pp. 521–537.

Hsiao, G.; Schnack, E.; Wendland, W. (2000b): Hybrid coupled finite-boundary element methods for elliptic systems of second order. *Comput. Methods Appl. Mech. Engrg.*, vol. 190, pp. 431–485.

Jaswon, M. A.; Symm, G. T. (1977): *Integral Equation Methods in Potential Theory and Elastostatics*. Academic Press, London.

Jiao, X.; M.T.Heath (2004): Common-refinement based data transfer between non-matching meshes in multiphysics simulations. *Int. J. Num. Meth. Engrg.*, vol. 61, pp. 2402–2427.

Maier, G.; Diligenti, M.; Carini, A. (1991): A variational approach to boundary element elastodynamic analysis and extension to multidomains problems. *Comput. Methods Appl. Mech. Engrg.*, vol. 92, pp. 193 – 213.

Mantič, V.; París, F. (1995): Existence and evaluation of the free terms in the hypersingular boundary integral equation of potential theory. *Eng. Anal. Bound. Elem.*, vol. 16, pp. 253–260.

Mantič, V.; París, F. (1997a): Symmetrical representation of stresses in the Stroh formalism and its application to a dislocation and a dislocation dipole in an anisotropic medium. *J. Elast.*, vol. 47, pp. 101–120.

Mantič, V.; París, F. (1997b): Symmetry properties of the kernels of the hypersingular integral and the corresponding regularized integral in the 2D Somigliana stress identity for isotropic materials. *Eng. Anal. Bound. Elem.*, vol. 20, pp. 63–168.

McDevitt, T.; Laursen, T. (2000): A mortar-finite element formulation for frictional contact problems. *Int. J. Num. Meth. Engrg.*, vol. 48, pp. 1525–1547.

Núñez, J.; Muñoz, D.; Mantič, V.; París, F. (2003): A weak application of transmission conditions in 2D BEM with non-conforming meshes

for isotropic and anisotropic potential problems. In Gallego, R.; Aliabadi, M. (Eds): *Advances in Boundary Element Techniques IV*, pp. 111–116.

Panzeca, T.; Salerno, M.; Terravechia, S. (2002): Domain decomposition in the symmetric boundary element analysis. *Comput. Mech.*, vol. 28, pp. 191 – 201.

París, F.; Cañas, J. (1997): *Boundary Element Method, Fundamentals and Applications*. Oxford University Press, Oxford.

Puso, M. (2004): A 3D mortar method for solid mechanics. *Int. J. Num. Meth. Engrg.*, vol. 59, pp. 315–336.

Qian, Z.; Han, Z.; Atluri, S. (2004): Directly derived non-hyper-singular boundary integral equations for acoustic problems, and their solution through Petrov-Galerkin schemes. *CMES : Computer Modeling in Engineering and Sciences*, vol. 5, pp. 541–562.

Quarteroni, A.; Valli, A. (1999): *Domain decomposition methods for partial differential equations*. Oxford University Press, Oxford.

Schnack, E. (1987): A hybrid BEM model. *Int. J. Num. Meth. Engrg.*, vol. 24, pp. 1015–1025.

Sirtori, S. (1979): General stress analysis by means of integral equations and boundary elements. *Meccanica*, vol. 14, pp. 210–218.

Springhetti, R.; Novati, G.; Margonari, M. (2004): Weak coupling of the symmetric Galerkin BEM with FEM for potential and elastostatic problems. *CMES: Computer Modeling in Engineering and Sciences*, vol. 13, pp. 67–80.

Steinbach, O. (2003): *Stability estimates for hybrid coupled domain decomposition methods*. Springer-Verlag, Berlin Heidelberg.

Vodička, R. (2000): The first-kind and the second-kind boundary integral equation systems for solution of frictionless contact problems. *Eng. Anal. Bound. Elem.*, vol. 24, pp. 407–426.

Vodička, R.; Mantič, V. (2004): On invertibility of elastic single layer potential operator. *J. Elast.*, vol. 74, pp. 147–173.

Vodička, R.; Mantič, V.; París, F. (2006): On the removal of the non-uniqueness in the solution of elastostatic problems by symmetric Galerkin BEM. *Int. J. Num. Meth. Engrg.*, vol. 66, pp. 1884 – 1912.

Wendland, W.; Hsiao, G. (2004): Boundary element methods: Foundation and error analysis. In E. Stein, R. De Borst, T.J.R. Hughes(Ed): *Encyclopedia of Computational Mechanics, Vol. 1 Fundamentals*. John Wiley, New York, pp. 339-373.

Young, A. (1996): A single-domain boundary element method for 3-D elastostatic crack analysis using continuous elements. *Int. J. Num. Meth. Engrg.*, vol. 39, pp. 1265–1293.

Appendix A Analysis of the SGBEM formulation for a DDBVP with a single boundary

The aim of this Appendix is to show how the discretized system (25) reduces to its Schur complement and to analyze the reduced system obtained. Although, for the sake of clarity, a simple DDBVP with $\Omega = R^2$ partitioned to an interior (bounded) subdomain Ω^A and an exterior (unbounded) subdomain Ω^B separated by a bounded interface curve, Figure A1(a), is considered, it is expected that the conclusions deduced from the following analysis can be extended to other more complex problems.

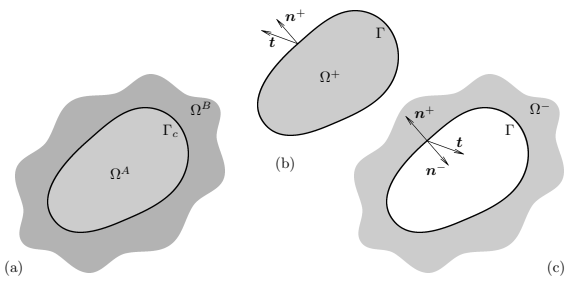

Figure A1: (a) A domain decomposition. Interior (b) and exterior (c) domains and pertinent normal vectors.

Appendix A.1 Preliminaries. Steklov-Poincaré operator.

Let us summarize, first, some of the representation formulas of the symmetric Steklov-Poincaré operator $\mathfrak{S}$, known also as the Dirichlet-Neumann map [Quarteroni and Valli (1999); Hsiao *et al.* (2000b); Steinbach (2003)]. In the case of elasticity, it is a map of boundary displacements u to boundary tractions t. It will be useful to represent this map by the boundary integral operators which appear in (5a) and (5b). First, let us rewrite those equations in operator form, using the notation:

$$(Zw)_j(y) = \int_\Gamma Z_{ji}(y,x) w_i(x) \mathrm{d}_x S, \tag{A1}$$

where w stands for u or t, Z stands for U, T, T^* or S and Γ is the boundary of a bounded domain Ω^+, see Figure A1(b) or of an unbounded domain Ω^-, see Figure A1(c). The integral in (A1) can be weakly singular, Cauchy principal value or Hadamard finite part integral. Equations (5a) and (5b) can respectively be represented by the following operator equations:

$$Ut = \left(T^{\pm} + \frac{1}{2}I\right) u \quad \text{and} \quad \left(T^{*\pm} - \frac{1}{2}I\right) t = Su, \tag{A2}$$

where the introduced symbol $T^{\pm}$ specifies that the pertinent operator is evaluated with respect to one of the normals $n^{\pm}$, respectively. Thus, for the interior problem the '+' sign is used whereas '-' is used for the exterior one, see Figure A1(b), (c). Recall also that the form of these equations is the same for both interior and exterior problems, providing the condition at infinity (3) is satisfied.

In what follows it will also be useful to solve the exterior problem with tractions evaluated with respect to the normal n^+. In this case, everything which depends on this choice changes its sign. Therefore, t changes to $-t$ and T^- is converted to $-T^+$. Equations (A2) take the form:

$$Ut = \left(T^{+} - \frac{1}{2}I\right) u \quad \text{and} \quad \left(T^{*+} + \frac{1}{2}I\right) t = Su. \tag{A3}$$

A couple of representations of the operator $\mathfrak{S}$ are described in the following. Applying the inverse of the operator U, which exists in 3D always and in 2D if the problem is suitably scaled [Vodička and Mantič (2004)], to $(A2)_1$ a nonsymmetric representation of $\mathfrak{S}$ is obtained:

$$t = U^{-1}\left(T^{\pm} + \frac{1}{2}I\right) u = \mathfrak{S}u, \tag{A4}$$

while substituting this representation into $(A2)_2$ leads to its symmetric representation:

$$t = \left(\left(T^{*\pm} + \frac{1}{2}I\right) U^{-1}\left(T^{\pm} + \frac{1}{2}I\right) - S\right) u = \mathfrak{S}u. \tag{A5}$$

There exists one important difference between the operators $\mathfrak{S}$ defined for the interior and exterior BVPs. That for the interior BVP is not invertible, though positive semi-definite, as any rigid body motion gives zero tractions, while the other, for the exterior BVP, is invertible and positive definite (in 2D only if the domain is suitably scaled [Vodička and Mantič (2004)]). The operator $T + \frac{1}{2}I$ (and its adjoint counterpart as well) also has a similar property of invertibility: $T^- + \frac{1}{2}I$ is invertible whereas $T^+ + \frac{1}{2}I$ is not invertible.

Both aforementioned representations of $\mathfrak{S}$ for the exterior BVP can be rewritten using the normal n^+, denoting the operator as $\mathfrak{S}_{ex}$, so equation $(A3)_1$ leads to:

$$t = U^{-1}\left(T^{+} - \frac{1}{2}I\right) u = \mathfrak{S}_{ex}u, \tag{A6}$$

while substituting this representation into $(A3)_2$ results in its symmetric representation:

$$t = \left(-\left(T^{*+} - \frac{1}{2}I\right) U^{-1}\left(T^{+} - \frac{1}{2}I\right) + S\right) u = \mathfrak{S}_{ex}u. \tag{A7}$$

In a similar way the normal n^- can be used in representations of $\mathfrak{S}$ for the interior BVP.

Appendix A.2 Schur complement

Let the load in a DDBVP defined in Figure A1(a) be given, for simplicity, by some finite volume

forces having a bounded support in Ω^B. Thus, the formula $(3)_1$ still holds. The presence of these volume forces leads to a modification of the right-hand side in the resulting system of linear equations, introduced originally in (25) without body forces. For the problem in Figure A1(a) the vector representing boundary conditions on the right-hand side of (25) vanishes, and the only contribution to the right-hand side of the resulting system is given by a contribution of volume forces, denoted here by vectors h_f^B and g_f^B. Thus, the resulting system of equations for the problem in Figure A1(a) can be expressed in block form as:

$$\begin{pmatrix} MATRIX \\ V \end{pmatrix} \begin{pmatrix} \mathrm{t}^A \\ \mathrm{u}^A \\ \mathrm{t}^B \\ \mathrm{u}^B \end{pmatrix} = \begin{pmatrix} 0 \\ 0 \\ \mathrm{h}_f^B \\ \mathrm{h}_f^B \end{pmatrix}, \tag{A8}$$

$$\begin{pmatrix} MATRIX \\ V \end{pmatrix} = \begin{pmatrix} -\mathrm{U}^A & -\frac{1}{2}\mathrm{M}^A+\mathrm{T}^A & 0 & \mathrm{M}^{AB} \\ -\frac{1}{2}\mathrm{M}^{AT}+\mathrm{T}^{AT} & -\mathrm{S}^A & 0 & 0 \\ 0 & 0 & -\mathrm{U}^B & \frac{1}{2}\mathrm{M}^B+\mathrm{T}^B \\ \mathrm{M}^{ABT} & 0 & \frac{1}{2}\mathrm{M}^{BT}+\mathrm{T}^{BT} & -\mathrm{S}^B \end{pmatrix},$$

where we have omitted the redundant subscript c.

The Schur complement [Quarteroni and Valli (1999)] of the above system will be deduced in what follows, to see which unknowns can be eliminated in a natural way. The non-eliminated unknowns will represent primary unknowns which can be used to recover the remaining unknowns.

For simplicity in some of the following expressions, we will assume hereinafter that dimensions of the spaces generated by boundary element shape functions for diplacements and tractions on one subdomain coincide. Hence, M^A and M^B are square matrices. Moreover, let the pertinent spaces be such that these matrices have full rank, thus being invertible.

Performing the block-Gaussian elimination in the first column in (A8), the left-hand side matrix is obtained in the form:

$$\begin{pmatrix} MATRIX & MATRIX \\ VI & VII \end{pmatrix} \tag{A9}$$

where

$$\begin{pmatrix} MATRIX \\ VI \end{pmatrix} = \begin{pmatrix} \mathrm{I}^A & -\mathrm{U}^{A\,-1}\left(-\frac{1}{2}\mathrm{M}^A+\mathrm{T}^A\right) \\ 0 & \left(-\frac{1}{2}\mathrm{M}^{AT}+\mathrm{T}^{AT}\right)\mathrm{U}^{A\,-1}\left(-\frac{1}{2}\mathrm{M}^A+\mathrm{T}^A\right)-\mathrm{S}^A \\ 0 & 0 \\ 0 & \mathrm{M}^{ABT}\mathrm{U}^{A\,-1}\left(-\frac{1}{2}\mathrm{M}^A+\mathrm{T}^A\right) \end{pmatrix},$$

$$\begin{pmatrix} MATRIX \\ VII \end{pmatrix} = \begin{pmatrix} 0 & -\mathrm{U}^{A\,-1}\mathrm{M}^{AB} \\ 0 & \left(-\frac{1}{2}\mathrm{M}^{AT}+\mathrm{T}^{AT}\right)\mathrm{U}^{A\,-1}\mathrm{M}^{AB} \\ -\mathrm{U}^B & \frac{1}{2}\mathrm{M}^B+\mathrm{T}^B \\ \frac{1}{2}\mathrm{M}^{BT}+\mathrm{T}^{BT} & \mathrm{M}^{ABT}\mathrm{U}^{A\,-1}\mathrm{M}^{AB}-\mathrm{S}^B \end{pmatrix}.$$

The term in the first row of the second column of this matrix is, according to (A6), a Galerkin discretization of a nonsymmetric representation of the local Steklov-Poincaré operator for the domain exterior to Ω^A, denoted hereinafter as:

$$\mathcal{S}^A_{ex,n} = \mathrm{U}^{A\,-1}\left(-\frac{1}{2}\mathrm{M}^A+\mathrm{T}^A\right). \tag{A10}$$

Inasmuch as the local Steklov-Poincaré operator for the exterior BVP is invertible, the matrix $\mathcal{S}^A_{ex,n}$ is assumed to be nonsingular. However, the symmetry of the operator $\mathfrak{S}^A_{ex}$ may not be maintained at the discretized level. Actually, using concepts of dual basis of spaces generated by boundary element shape functions (for tractions and displacements) and generalized L_2-projections (defined using Galerkin-Petrov scheme) onto these finite dimensional spaces [Steinbach (2003)], it can be shown that the following relation may hold only approximately:

$$\begin{aligned} &\mathrm{U}^{A\,-1}\left(-\frac{1}{2}\mathrm{M}^A+\mathrm{T}^A\right)\mathrm{M}^{A\,-1} \\ &\simeq \left(\mathrm{M}^{AT}\right)^{-1}\left(-\frac{1}{2}\mathrm{M}^{AT}+\mathrm{T}^{AT}\right)\mathrm{U}^{A\,-1}, \end{aligned} \tag{A11}$$

although it holds at the operator level, see Wendland and Hsiao (2004):

$$U^{A\,-1}\left(-\frac{1}{2}I^A+T^A\right) = \left(-\frac{1}{2}I^A+T^{A\,*}\right)U^{A\,-1}. \tag{A12}$$

The second diagonal term equals, up to the sign, a Galerkin discretization of a symmetric representation of the local Steklov-Poincaré operator for

the domain exterior to Ω^A. Thus, the following symmetric matrix is assumed to be nonsingular:

$$\mathcal{S}^A_{ex,s} = -\left(-\frac{1}{2}\mathrm{M}^{AT}+\mathrm{T}^{AT}\right)\mathrm{U}^{A-1}\left(-\frac{1}{2}\mathrm{M}^{A}+\mathrm{T}^{A}\right) + \mathrm{S}^A. \quad \text{(A13)}$$

Though the matrices $\mathcal{S}^A_{ex,s}$ and $\mathcal{S}^A_{ex,n}$ represent the same local Steklov-Poincaré operator, due to the discretization they may equal each other only approximately, and moreover the latter may be nonsymmetric. Applying the notation introduced in (A10) and (A13) to (A9) results in the the following form of the system:

$$\begin{pmatrix} MATRIX \\ VIII \end{pmatrix}\begin{pmatrix} \mathrm{t}^A \\ \mathrm{u}^A \\ \mathrm{t}^B \\ \mathrm{u}^B \end{pmatrix} = \begin{pmatrix} 0 \\ 0 \\ \mathrm{h}^B_f \\ \mathrm{g}^B_f \end{pmatrix}, \quad \text{(A14)}$$

where

$$\begin{pmatrix} MATRIX \\ VIII \end{pmatrix} = \begin{pmatrix} \mathrm{I}^A & -\mathcal{S}^A_{ex,n} & 0 & -\mathrm{U}^{A-1}\mathrm{M}^{AB} \\ 0 & -\mathcal{S}^A_{ex,s} & 0 & \mathcal{S}^{AT}_{ex,n}\mathrm{M}^{AB} \\ 0 & 0 & -\mathrm{U}^B & \frac{1}{2}\mathrm{M}^B+\mathrm{T}^B \\ 0 & \mathrm{M}^{ABT}\mathcal{S}^A_{ex,n} & \frac{1}{2}\mathrm{M}^{BT}+\mathrm{T}^{BT} & \mathrm{M}^{ABT}\mathrm{U}^{A-1}\mathrm{M}^{AB}-\mathrm{S}^B \end{pmatrix}.$$

After eliminating the terms under the diagonal in the second and third columns of (A14) the following system is obtained:

$$\begin{pmatrix} MATRIX \\ IX \end{pmatrix}\begin{pmatrix} \mathrm{t}^A \\ \mathrm{u}^A \\ \mathrm{t}^B \\ \mathrm{u}^B \end{pmatrix} = \begin{pmatrix} 0 \\ 0 \\ -\mathrm{U}^{B-1}\mathrm{h}^B_f \\ \mathcal{S}^{BT}_n\mathrm{h}^B_f + \mathrm{g}^B_f \end{pmatrix}, \quad \text{(A15)}$$

with

$$\begin{pmatrix} MATRIX \\ IX \end{pmatrix} = \begin{pmatrix} \mathrm{I}^A & -\mathcal{S}^A_{ex,n} & 0 & -\mathrm{U}^{A-1}\mathrm{M}^{AB} \\ 0 & \mathrm{I}^A & 0 & -\mathcal{S}^{A-1}_{ex,s}\mathcal{S}^{AT}_{ex,n}\mathrm{M}^{AB} \\ 0 & 0 & \mathrm{I}^B & -\mathcal{S}^B_n \\ 0 & 0 & 0 & \mathcal{S}^B_s+\mathrm{M}^{ABT}\left(\mathcal{S}^A_{ex,n}\mathcal{S}^{A-1}_{ex,s}\mathcal{S}^{AT}_{ex,n}+\mathrm{U}^{A-1}\right)\mathrm{M}^{AB} \end{pmatrix},$$

where the Galerkin discretizations of nonsymmetric and symmetric representations of the local Steklov-Poincaré operator for Ω^B, respectively, have been denoted as:

$$\mathcal{S}^B_n = \mathrm{U}^{B-1}\left(\frac{1}{2}\mathrm{M}^B+\mathrm{T}^B\right), \quad \text{(A16)}$$

$$\mathcal{S}^B_s = \left(\frac{1}{2}\mathrm{M}^{BT}+\mathrm{T}^{BT}\right)\mathrm{U}^{B-1}\left(\frac{1}{2}\mathrm{M}^B+\mathrm{T}^B\right)-\mathrm{S}^B. \quad \text{(A17)}$$

Since Ω^B is an exterior subdomain, these matrices are assumed to be nonsingular, the symmetric one being positive definite.

The last diagonal term in (A15) is the Schur complement matrix. To analyze the meaning of the expression in parentheses in this term it is useful to write it in terms of operators:

$$\begin{aligned} \mathfrak{S}^A_{ex}\mathfrak{S}^{A-1}_{ex}\mathfrak{S}^A_{ex}+U^{A-1} &= \mathfrak{S}^A_{ex}+U^{A-1} \\ &= U^{A-1}\left(T^{A+}-\frac{1}{2}I^A\right)+U^{A-1} \\ &= U^{A-1}\left(T^{A+}+\frac{1}{2}I^A\right) \\ &= \mathfrak{S}^A. \end{aligned} \quad \text{(A18)}$$

Therefore, the expression in parentheses corresponds to a discretization of a somewhat more complicated symmetric representation of $\mathfrak{S}^A$ than its 'standard' symmetric representation:

$$\mathcal{S}^A_s = \left(\frac{1}{2}\mathrm{M}^{AT}+\mathrm{T}^{AT}\right)\mathrm{U}^{A-1}\left(\frac{1}{2}\mathrm{M}^A+\mathrm{T}^A\right)-\mathrm{S}^A. \quad \text{(A19)}$$

It will be denoted as:

$$\mathcal{S}^A_{in,s} = \mathcal{S}^A_{ex,n}\mathcal{S}^{A-1}_{ex,s}\mathcal{S}^{AT}_{ex,n}+\mathrm{U}^{A-1}. \quad \text{(A20)}$$

Then, the reduced Schur complement system obtained from (A8) in (A15) reads:

$$\left(\mathcal{S}^B_s+\mathrm{M}^{ABT}\mathcal{S}^A_{in,s}\mathrm{M}^{AB}\right)\mathrm{u}^B = \mathcal{S}^{BT}_n\mathrm{h}^B_f+\mathrm{g}^B_f. \quad \text{(A21)}$$

The Schur complement matrix on the left-hand side of (A15) is a symmetric positive definite matrix, since $\mathcal{S}^B_s$ is symmetric positive definite and

$\mathcal{S}^A_{in,s}$ is symmetric positive semi-definite. Hence, vector u^B can be found uniquely.

The complete solution of the system (A8) can be obtained from u^B by backward substitution in (A15) giving:

$$\mathrm{t}^B = \mathcal{S}^B_n \mathrm{u}^B - \mathrm{U}^{B\,-1}\mathrm{h}^B_f, \tag{A22}$$

$$\mathrm{u}^A = \mathcal{S}^{A\,-1}_{ex,s}\mathcal{S}^{A\,T}_{ex,n}\mathrm{M}^{AB}\mathrm{u}^B, \tag{A23}$$

$$\mathrm{t}^A = \mathcal{S}^A_{in,s}\mathrm{M}^{AB}\mathrm{u}^B. \tag{A24}$$

It has to be stressed that vector u^B represents naturally primary unknowns in the reduced Schur complement system associated to the full system (A8). This is associated to the fact that for non-matching discretizations of Γ_c the interface mass matrix M^{AB} appearing in relations (A23-A24) is in general not a square matrix. Thus, *e.g.*, one cannot in general express u^B in terms of u^A inverting the relation (A23).

To express t^A through u^A it is sufficient to substitute $\mathrm{M}^{AB}\mathrm{u}^B$ obtained from (A23) into (A24) resulting in:

$$\mathrm{t}^A = \mathcal{S}^A_{in,s}\left(\mathcal{S}^{A\,T}_{ex,n}\right)^{-1}\mathcal{S}^A_{ex,s}\mathrm{u}^A. \tag{A25}$$

With the aid of (A20), (A13) and (A10) in the respective order, relation (A25) can be substantially simplified:

$$\begin{aligned}\mathrm{t}^A &= \left(\mathcal{S}^A_{ex,n} + \mathrm{U}^{A\,-1}\left(\mathcal{S}^{A\,T}_{ex,n}\right)^{-1}\mathcal{S}^A_{ex,s}\right)\mathrm{u}^A \\ &= \left(\mathcal{S}^A_{ex,n} + \left(-\frac{1}{2}\mathrm{M}^{A\,T} + \mathrm{T}^{A\,T}\right)^{-1}\mathcal{S}^A_{ex,s}\right)\mathrm{u}^A \\ &= \left(-\frac{1}{2}\mathrm{M}^{A\,T} + \mathrm{T}^{A\,T}\right)^{-1}\mathrm{S}^A\mathrm{u}^A.\end{aligned} \tag{A26}$$

The matrix in the last term, denoted as $\mathcal{S}^A_{in,n}$, gives the Galerkin discretization of another non-symmetric representation of the local Steklov-Poincaré operator for Ω^A, due to $(\mathrm{A2})_2$. Recall that the matrix $-\frac{1}{2}\mathrm{M}^{A\,T} + \mathrm{T}^{A\,T}$ is a discretization of an invertible operator $-\frac{1}{2}I + T^+$ defined on the boundary of Ω^A, see Appendix. Therefore, (A25) can be written as:

$$\mathrm{t}^A = \mathcal{S}^A_{in,n}\mathrm{u}^A. \tag{A27}$$

Note that the choice of Ω^A as an exterior domain in the present DDBVP (contrary to what has been done in the above study) would lead to a singular system matrix in (A8), due to the vanishing product of any rigid body displacement u^A times the second column of this matrix. In order to obtain a nonsingular system matrix in such a case some of the techniques introduced in Vodička *et al.* (2006) could be applied, as already mentioned in Section 5.3.3.

Appendix A.3 Influence of the choice of the interface sides A and B on traction oscillations

Displacement and traction solution computed along the interface at the finer mesh when this mesh is placed on the Ω^A side presents oscillations not observed in solutions at other meshes, see Section 5.3. An explanation of this observation will be introduced here using the results of the previous section.

As follows from (A21) and (A22-A24) the nodal values of u^B can be considered as the primary values in the solution of system (A8). It will be shown that the matrix operator computing u^A from u^B, according to relation (A23), can be considered as an approximation of a projection from the space of the displacement nodal values on the Ω^B side of Γ_c to the displacement nodal values on the Ω^A side. First, let us evaluate the product of the inverse matrix and the matrix associated to two different representations of the local Steklov-Poincaré operator for the domain exterior to Ω^A in (A23):

$$\begin{aligned}&\mathcal{S}^{A\,-1}_{ex,s}\mathcal{S}^{A\,T}_{ex,n} = \left(\mathcal{S}^{A\,T\,-1}_{ex,n}\mathcal{S}^A_{ex,s}\right)^{-1} \\ &= \left[\mathrm{U}^A\left(-\frac{1}{2}\mathrm{M}^{A\,T} + \mathrm{T}^{A\,T}\right)^{-1}\left(-\left(-\frac{1}{2}\mathrm{M}^{A\,T} + \mathrm{T}^{A\,T}\right)\right.\right. \\ &\qquad \left.\left.\cdot\,\mathrm{U}^{A\,-1}\left(-\frac{1}{2}\mathrm{M}^A + \mathrm{T}^A\right) + \mathrm{S}^A\right)\right]^{-1} \\ &= \left[-\left(-\frac{1}{2}\mathrm{M}^A + \mathrm{T}^A\right) + \mathrm{U}^A\left(-\frac{1}{2}\mathrm{M}^{A\,T} + \mathrm{T}^{A\,T}\right)^{-1}\mathrm{S}^A\right]^{-1}\end{aligned} \tag{A28}$$

$$\overset{(A11)}{\cong}\left[-\left(-\frac{1}{2}\mathrm{M}^A+\mathrm{T}^A\right)+\mathrm{M}^A\left(-\frac{1}{2}\mathrm{M}^A+\mathrm{T}^A\right)^{-1}\cdot\mathrm{U}^A\left(\mathrm{M}^{AT}\right)^{-1}\mathrm{S}^A\right]^{-1}$$

$$\overset{(A30)}{\cong}\left[-\left(-\frac{1}{2}\mathrm{M}^A+\mathrm{T}^A\right)+\mathrm{M}^A\left(-\frac{1}{2}\mathrm{M}^A+\mathrm{T}^A\right)^{-1}\cdot\left(\left(-\frac{1}{2}\mathrm{M}^A+\mathrm{T}^A\right)\mathrm{M}^{A-1}\left(\frac{1}{2}\mathrm{M}^A+\mathrm{T}^A\right)\right)\right]^{-1}$$

$$=\mathrm{M}^{A-1}, \tag{A29}$$

which may be valid only approximately due to the two in general only approximately valid equations used: (A11), which proclaims that the matrix $\mathcal{S}^A_{ex,n}\mathrm{M}^{A-1}$ is symmetric, and

$$\mathrm{U}^A\left(\mathrm{M}^{AT}\right)^{-1}\mathrm{S}^A \simeq\left(-\frac{1}{2}\mathrm{M}^A+\mathrm{T}^A\right)\mathrm{M}^{A-1}\left(\frac{1}{2}\mathrm{M}^A+\mathrm{T}^A\right), \tag{A30}$$

which holds at the operator level, see Wendland and Hsiao (2004):

$$U^AS^A=\left(-\frac{1}{2}I^A+T^A\right)\left(\frac{1}{2}I^A+T^A\right), \tag{A31}$$

Thus, equation (A23) can be approximated by the relation:

$$\mathrm{u}^A\cong\mathrm{M}^{A-1}\mathrm{M}^{AB}\mathrm{u}^B=\mathrm{Q}^{AB}\mathrm{u}^B, \tag{A32}$$

where the matrix Q^{AB} is the matrix of the L_2-projection operator of the space of boundary element shape functions defined on Γ^B onto the one defined on Γ^A. Therefore, if the matrix Q^{AB} has more rows than columns, i.e. if $N^A>N^B$, a 'linearization' of the results may occur as shown in Figure 6.

The following illustrative examples simulate the effect of the choice of the interface side where the finer-coarser mesh is defined. Consider the two non-matching mesh patterns 2–5 and 3–7 used in examples of Section 5, see Figures 6 and 14(top). First, taking $N^A>N^B$, let a quadratic function f be approximated at the coarser meshes, see Figure A2, by a random perturbation of nodal values of the piecewise linear interpolation of f. The projection of these approximations at the coarser meshes by means of the matrices Q^{AB} onto approximations at the finer meshes are plotted in Figure A2 as well. It can be observed that the approximations at the finer meshes lie very close to the piecewise linear approximation given by the coarser meshes.

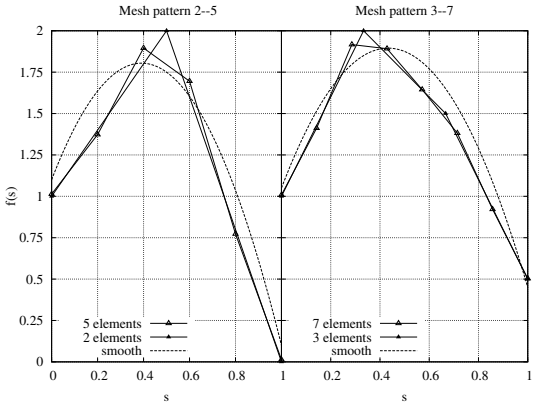

Figure A2: Projection from the coarser mesh to the finer one.

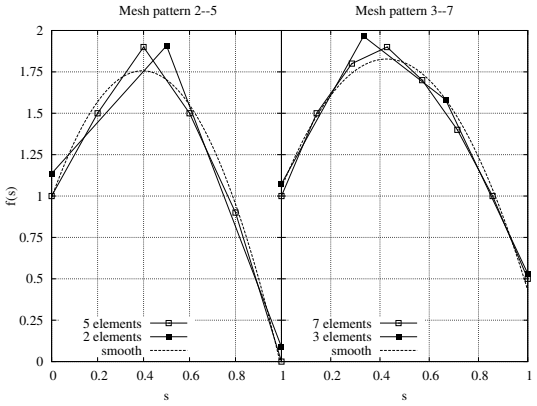

Figure A3: Projection from the finer mesh to the coarser one.

In the opposite situation, with $N^A<N^B$, this 'linearization' does not happen, but a piecewise linear smoothing of the possibly oscillating data can take place, see Figure A3.

The traction nodal values can be evaluated from the displacement ones using (A22) and (A27). The matrices which appear in these relations are

the Galerkin discretizations of some representations of the local Steklov-Poincaré operators. Such operators, which actually perform differentiation, decrease solution smoothness. Therefore, the oscillations in traction errors can be expected to be much higher than in the case of the corresponding displacements, which has actually been observed.